Materials Today Energy 14 (2019) 100332

Contents lists available at ScienceDirect

Materials Today Energy

journal homepage: www.journals.elsevier.com/materials-today-energy/

Synthetic control of Prussian blue derived nano-materials for energy storage and conversion application

Yiwei Li [1], Jiangtao Hu [1], Kai Yang, Bo Cao, Zhibo Li, Luyi Yang[**], Feng Pan[*]

School of Advanced Materials, Peking University, Shenzhen Graduate School, Shenzhen 518055, People's Republic of China

ARTICLE INFO

Article history:
Received 22 May 2019
Received in revised form
18 July 2019
Accepted 29 July 2019
Available online 11 September 2019

Keywords:
Prussian blue
Nano-materials
Batteries
Catalysts
Super-capacitors

ABSTRACT

As a presentative material of metal-organic frameworks (MOFs), Prussian blue (PB) draws great attention due to its low cost, facile preparation processes and hollow framework structure. Previous studies show that the PB-derived nanomaterials can inherit part of their features, exhibiting large surface area, inter-connected pores and hierarchical pore sizes, which may promote charge transfer when utilized in energy storage and conversion system. By tuning synthesis conditions (e.g. temperature and atmosphere), nano-materials with desirable structures and properties can be obtained, leading to various usage areas for energy storage and conversion applications (e.g. batteries, supercapacitors and catalysts). In this work, for the first time, various products obtained under different preparation conditions and their applications are summarized in detail in order to offer guiding significance for synthesizing nanoporous materials with special purposes.

© 2019 Elsevier Ltd. All rights reserved.

1. Introduction

In order to meet the urgent demand for clean energy storage and conversion systems, lithium/sodium ion batteries (LIBs, SIBs), flow cells, super-capacitors, catalysis et al., have been widely investigated [1–5]. To realize high-performance energy system, the major challenge is to explore appropriate energy materials [2].

Composed of metal cations lattice point linked by organic ligands, metal-organic frameworks (MOFs) have been widely investigated in energy field recently [6]. Generally, MOFs exhibit superior physical and chemical properties, such as high specific surfaces areas [7], porosity [8], electrochemical activity [9], magnetic properties [10], adsorption [11], biocompatibility [12] and selectivity [13]. Due to the excellent properties, the MOFs have been widely used in catalysis [14], drug controlled release system [15], synthesis and separation [16], especially in energy conversion and storage systems [17], including LIBs [18], SIBs [19] and super-capacitors [20]. Prussian blue analogues (PBAs) are the representative materials among various types of MOFs. The general chemical formula of PBA could be described as $A_lM_n[\acute{M}_m(CN)_6].xH_2O$, where A represents alkali metal ions like Na^+ and K^+, M and Ḿ represent transition metal cations. PBA generally exhibits cubic structures, where the cyanide groups act as bridges connecting the transition metal ions, as shown in Fig. 1a [21]. Owing to the special structure where two types of metal centers in the octahedral sites linked by cyanide chains, it has been widely used in gas storage [22], alkali metal ions batteries [23], catalysis [24], energy separation [25], charge transfer [26], drug delivery [27] and sensors [28].

In PBA, the transition metal cations M and Ḿ could be manganese [30], cobalt [31], nickel [31], copper [32] and zinc [33] without breaking the crystal structure. When both M and Ḿ are iron, the final composition will be $Fe_4[Fe(CN)_6]_3.xH_2O$, which is generally known as Prussian blue (PB) or FeCNFe [34]. The PB has been known since 1704 and its structure has been researched since 1936 [115]. As shown in Fig. 1b, PB exhibits cubic structures; Fe^{2+} and Fe^{3+} are connected by cyanogens. Interestingly, all of Fe^{3+} are connected to the nitrogen atom of cyanide and all of Fe^{2+} are connected to the carbon atom of cyanide. PB could be categorized into soluble PB ($KFe[Fe(CN)_6]$) and insoluble PB ($Fe_4[Fe(CN)_6]_3$) [29]. Some defects exist in insoluble PB due to the interstitial water molecules, which could be divided into two types according to their coordination: the water molecules coordinated to M_{II} sites and the ones inside cavities which do not coordinate to metal sites. The lattice water molecules play an important part in stabilizing the structure of insoluble PB. If the lattice water molecules are removed

* Corresponding author.
** Corresponding author.
E-mail addresses: yangly@pkusz.edu.cn (L. Yang), panfeng@pkusz.edu.cn (F. Pan).
[1] These authors contributed equally to this work.

https://doi.org/10.1016/j.mtener.2019.07.003
2468-6069/© 2019 Elsevier Ltd. All rights reserved.

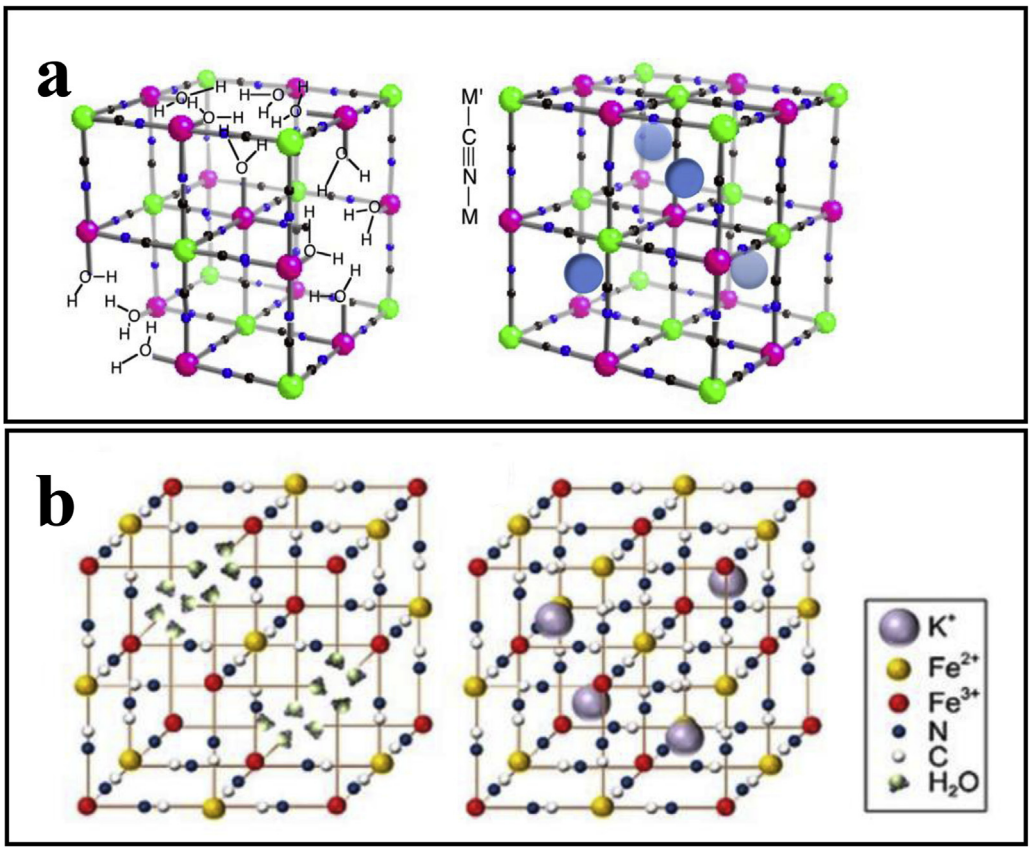

Fig. 1. (a) The illustrations of crystal structure of Prussian blue analogue alkali free ($x = 0$) and alkali in the tetrahedral sites ($x = 1$) [21]. (b) The illustrations of crystal structure of insoluble PB ($Fe_4[Fe(CN)_6]_3.xH_2O$, left) and soluble PB ($KFe[Fe(CN)_6]$, right) [29].

from the structure, the framework will collapse because it neutralizes the charges arising from defect octahedrons [35].

The detailed syntheses, structure and applications of PB have been systematically studied by Grandjean's group [116]. They mainly focused on the application of Prussian blue in dyes. PB has also been widely researched in alkaline metal ion batteries owning to its unique electrochemical properties. Shen et al. [36] synthesized two different PB materials ($Fe_4[Fe(CN)_6]_3$ and $FeFe(CN)_6$) used in LIBs, and Nie et al. [37] prepared flexible $Fe[Fe(CN)_6]$/carbon composite tested in SIBs, both of them exhibited super electrochemical performance. PB can be also utilized in multivalent ion batteries, such as magnesium ion batteries and calcium ion batteries [38,39]. More importantly, another potential application of PB is being used as precursors for the synthesis of nanostructured inorganic materials [40,41]. Final products with completely different properties can be obtained through synthetic tuning.

As shown in Fig. 2, the products derived from the thermal treatment of PB are largely decided by calcination atmosphere and temperature. The iron oxide with distinctive crystal structure and porosity could be prepared from PB under aerobic atmosphere, which is simple, inexpensive, tunable and scalable. The amorphous iron oxide obtained at low temperature will transform to crystal iron oxides with the increase of the temperature. Inheriting the unique crystal structure and porosity from PB, the iron oxides derived from PB normally exhibit large surface area, interconnected pores, and hierarchical pore sizes [42]. Different from the products in aerobic atmosphere, the products derived from PB under inert atmosphere are always contain C and N element [43]. At low temperature, the final products are mostly Fe_2O_3@N-doped C. With the temperature increasing, the iron and carbon will combine more closely and the final product will be Fe/Fe_3C@N-doped C. In addition, to further utilize the unique pore structure, the product derived from PB under inert atmosphere at low temperature was treated with acid [44]. Iron oxides are washed out with acid etching; therefore the final product is N-doped C with unique pore structure. All of these products derived from PB are widely utilized in energy storage fields, as shown in Fig. 2.

Owing to inheriting the porosity of PB, the iron oxides derived from PB will offer more void space which could buffer the volume variation and improve cycle stability compared to ordinary oxides anode in LIBs. For example, Zhang et al. [45] annealed PB via a facile solution method, which exhibits 800 mAh g^{-1} at 200 mA g^{-1} and 85% of the capacity preserved after 50 cycles when utilized as anode in LIBs. The Fe/Fe_3C@N-doped C has been widely used in catalysts field. Hu et al. [46] synthesized a Fe/Fe_3C wrapped by N-doped graphitic layers by calcining PB and glucose and utilized it as catalyst for Zn-air batteries. This work provides a simple way to synthesize Fe—N—C catalysts, which not only has superb catalytic performance but also a lower synthesize costs.

Since the products could inherit part of characteristics from PB, the thermal degradation of PB became an effective method to synthesis porous/hollow nanostructures. However, the final morphology and structure were determined by thermal treatment conditions and the properties of precursor, such as atmosphere, temperature, precursor size and other conditions. The morphology and structure of products derived from PB determine their appliance field to a great extent. Nevertheless, no reviews have been published to systematically sum up the products derived from PB through thermal treatment under different conditions. Herein, based on previous works, products derived from PB in different

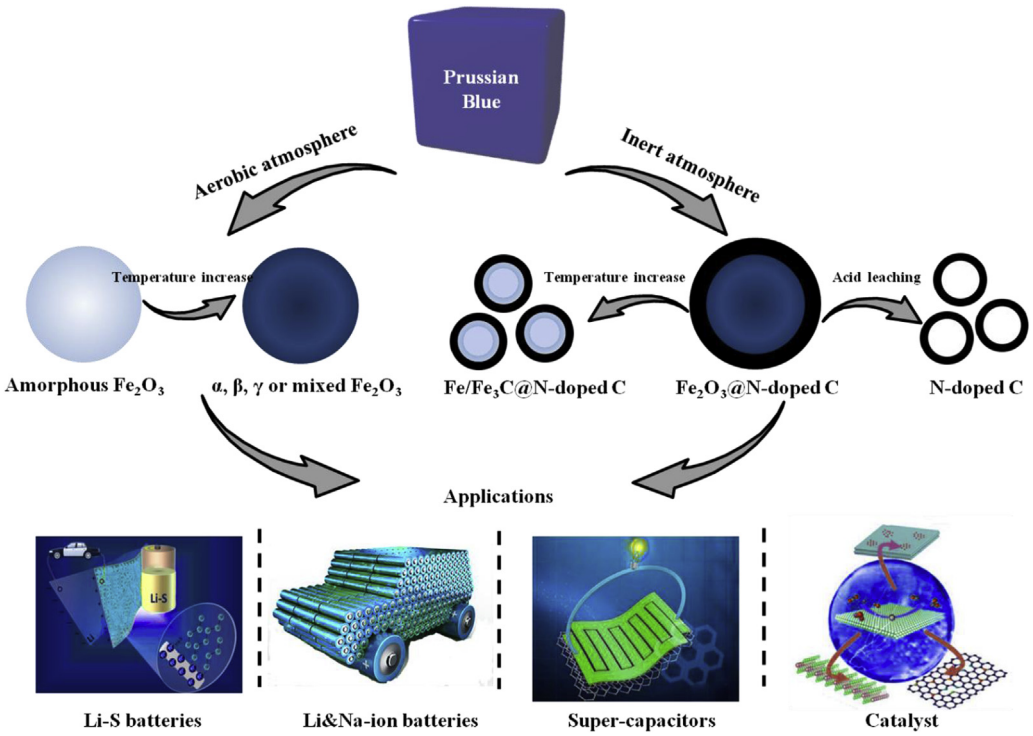

Fig. 2. The illustration of the products derived from PB at aerobic and inert atmosphere and their applications in energy storage fields.

synthetic conditions and their applications in energy storage field are summarized. This work has guiding significance for the future synthesis of nanoporous materials with special structure.

2. Pyrolysis products of PB and their applications in energy storage and conversion

The thermal degradation of PB is an effective method to obtain porous/hollow nanostructures. There are three distinct characteristics for thermal treatment products: morphology retention, pores formation and surface change. It has been previously reported that, after annealing, the cubic symmetry in crystal system could be well preserved [42]. Besides, during the process of annealing, the nano pores formed accompanied by the organic parts converted into gas and removed. The small nano pores connected with each other, forming big nano pores with airflow. With the formation of porous structures, the surface became rough owing to the small pores [47]. This method has some advantages compared to the traditional method [42]: on the one hand, nano-sized materials can be obtained at lower temperatures; on the other hand, inter-connecting hydrophobic nano pores can be formed, distinguished with “dead pores”.

The products after thermal treatment could be remarkably influenced by gas composition, temperature, reactant composition and gas pressure, especially gas composition and temperature [48]. In addition, owing to their unique properties; they have been widely utilized in energy storage field. In this review, we summarized the various annealing products derived from PB at different annealing temperature under aerobic atmosphere and inert atmosphere, and their applications in energy storage field.

2.1. Products obtained in aerobic atmosphere and their applications

2.1.1. Various calcined products in aerobic atmosphere

The PB will transform into iron oxide in different phases upon annealing in air, which could be a promising method to fabricate nano-porous iron oxide in large-scale production. As shown in Fig. 3a and b, after annealing, the cubic symmetry in crystal system could be well preserved. Fig. 3c displays the TGA curve of PB microcubes. Before heating up to 300 °C, a small amount of mass loss corresponding to the loss of crystalline water in the lattice of PB can be observed. Around 320 °C, obvious weight loss of PB nanocubes occurred, which means PB decomposed into iron oxide [49]. During heating, the cyanide skeleton fractured and transformed into carbon oxide and nitrogen oxide, then removed with air in the form of gas. At the same time, iron atoms, which lost the support, were oxidized and transformed into iron oxide. Zhang et al. [49] annealed PB at 350 °C, 550 °C and 650 °C respectively and found that the whole thermal transformation process could be divided into two major phases: Thermal decomposition of the PB microcubes (Fig. 3c) and further crystal growth of Fe_2O_3 (Fig. 3d). The β-Fe_2O_3 and γ-Fe_2O_3 obtained at 350 °C became more intense and sharper at 550 °C and 650 °C, corresponding to the crystal growth of Fe_2O_3. In addition, it was proposed that the process of the transformation of PB to iron oxide could be divided into three procedures in detail, as shown in Fig. 3e. As the temperature reach to 350 °C, the surface of PB start to transform to Fe_2O_3 and pore formed inside owing to Kirkendall effect. The whole process is accompanied by airflow from outside (Stage I). When the temperature reach to 550 °C, due to the crystal growth of iron oxide nanoparticles, some micro holes formed on the smooth and compact surfaces which contributed to the rough particle surface (Stage II). Finally, as the temperature reached 650 °C, porous iron oxide shell transformed to iron oxide nanosheet with layered structure (Stage III). Microcubes structure was retained owing to the cubic symmetry of crystal structure [49].

In this part, we summarized the thermal decomposition products of PB under aerobic atmosphere and relevant influencing factors, including annealing temperature, precursor particle size and pore structures, as shown in Table 1. Amorphous, α, β, γ and multiphase composite iron oxide could be obtained by controlling the parameters mentioned above.

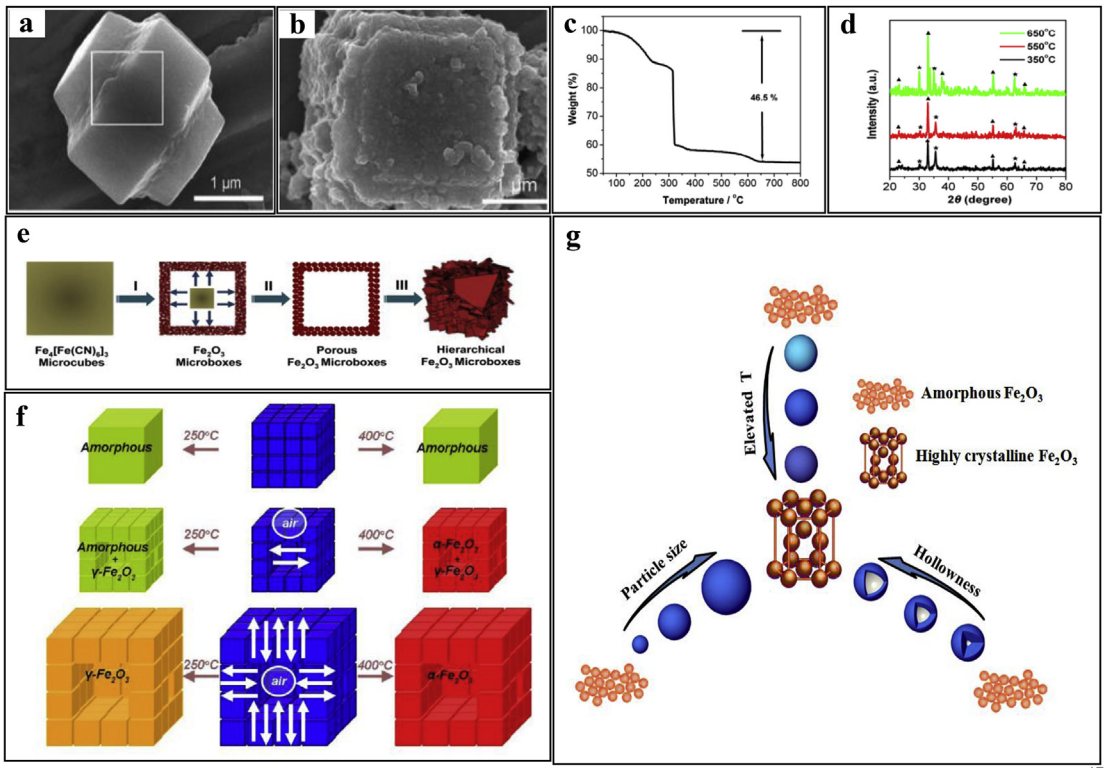

Fig. 3. (a) SEM image of as-prepared PB and (b) after thermal decomposition (iron oxide (III)) [47]. (c) TGA curve of PB in air flow. (d) XRD patterns of hollow Fe_2O_3 microboxes derived from PB at 350 °C, 550 °C and 650 °C. (▲: β-Fe_2O_3 and ★: γ-Fe_2O_3). (e) Illustration of the fabrication process of hollow Fe_2O_3 and its shell evolution with elevated temperature [49]. (f) Schematic diagram on thermal decomposition process of solid particles, small hollow particles and large hollow particles of PB at 250 °C and 400 °C [51]. (g) The summary of the changes in products with the increased annealing temperature, particle sizes and hollowness of the precursor.

To the best of our knowledge, the calcination temperature has a significant effect on the phase structure of the final products. Since crystallization process generally favours high temperatures, the annealing products tend to form amorphous phase at low temperature around 250 °C [50]. As the calcination temperature increases, the phase of the final products changes from amorphous to crystal, forming mixed crystalline phases in the intermediate temperature. Jiang et al. [53] calcined PB with a particle size about 450 nm at 350 °C, and mixed phases (α + γ-Fe_2O_3) was obtained. Zakaria et al. [55] calcined PB with a particle size around 80 nm at 400 °C, resulting in amorphous Fe_2O_3 + γ-Fe_2O_3. Hu et al. [47] calcined PB with a particle size of about 3 μm at 450 °C and the final product is β + γ-Fe_2O_3. When the temperature becomes even higher, the annealed products tend to be homogeneous phase structure. At the temperature above 600 °C, pure α-Fe_2O_3 can be obtained [56,57].

Table 1
The works of thermal decomposition of PB under aerobic atmosphere in recent years.

Temperature	PB size	Phase	Refs.
250 °C	60 nm	Amorphous Fe_2O_3	[50]
250 °C	100 nm	Amorphous Fe_2O_3	[51]
250 °C	100 nm	Amorphous Fe_2O_3 + γ-Fe_2O_3	[51]
250 °C	150 nm	γ-Fe_2O_3	[52]
350 °C	150 nm	β + γ-Fe_2O_3	[45]
350 °C	20 μm	β-Fe_2O_3	[48]
350 °C	450 nm	α + γ-Fe_2O_3	[53]
400 °C	20 nm	γ-Fe_2O_3	[54]
400 °C	80 nm	Amorphous Fe_2O_3 + γ-Fe_2O_3	[55]
400 °C	100 nm	α + γ-Fe_2O_3	[41]
400 °C	200 nm	α-Fe_2O_3	[51]
450 °C	3 μm	β + γ-Fe_2O_3	[47]
600 °C	300 nm	α-Fe_2O_3	[56]
650 °C	500 nm	α-Fe_2O_3	[57]

According to Table 1, we could generally summarize that with the increasing temperatures, the products with similar size will convert to phases with higher crystallinity. For instance, with the particle sizes of 100–150 nm, the lowest temperatures where amorphous, γ, β and α phase Fe_2O_3 can be formed are 250 °C, 250 °C, 350 °C and 400 °C, respectively [41,45,51,52]. This phenomenon is due to the increasing crystallinity of amorphous, γ, β and α phase. Nevertheless, there are still exceptions: Fe_2O_3 + γ-Fe_2O_3 can be formed under 400 °C with particle sizes of 80 nm, which may be due to other factors such as the speed of air flow or the compact level of precursor [55].

Other than temperature, the particle size will also affect the phase structure of the synthesized iron oxides after calcination. Two types of PB with different sizes were calcined at 350 °C [48]. After annealing, the smaller sized PB (10–15 nm) transformed into γ + α + amorphous Fe_2O_3; by contrast, the larger sized PB (20–50 μm) transformed into β + α Fe_2O_3. This is because the diffusing conditions of oxygen as well as the gas releasing processes during the decomposition of PB are different for different sized particles. Zhang et al. [45] and Jiang et al. [53] calcined PB particles with 150 nm and 450 nm, obtaining β + γ-Fe_2O_3 and α + γ-Fe_2O_3, respectively. The results above have indicated that the crystal structures of final products are also strongly dependent on the particle size of PB. In addition, it is also found that the products transform from γ phase to α phase with the particle sizes increase from 20 nm to 200 nm, which also demonstrates that the higher crystallinity phase could be obtained while using the bigger particles [51,54]. From the results above, one could speculate that

larger particle sizes normally result in higher crystallinity, which could be attributed to the smaller surface area, hence less defects. Generally speaking, products with higher crystallinity could be achieved through increasing the particle size. As shown in Table 1, with the increase of the particles sizes at 250 °C, the products transform from amorphous phase to γ phase [50–52]. However, we find that some samples mentioned above are not following this rule, because other conditions will also affect the final products [54,55].

Moreover, the phase structure of PB after thermal decomposition is also related to its degree of hollowness, which directly determines the thickness of iron source layer and further affects the crystallization degree of PB during thermal decomposition [50,58]. Hu et al. [51] calcined three kinds of PB with different hollowness and it is found that hollow structures can promote crystallization. As shown in Fig. 3f, solid particles, small hollow particles and large hollow particles of PB lead to different products at 250 °C. Accordingly, large degree of hollowness will promote the diffusion of airflow within the particle, which accelerates the process of crystallization; whereas the thick layers of iron source will block air diffusion during annealing, which contributes to the slow processes of oxidation rate and crystallization process.

As mentioned above, the products derived from PB in air are mainly porous Fe_2O_3. The crystal structures of the products are mainly controlled by three factors: temperature, particle sizes and hollow degree. Higher annealing temperature, larger particle sizes and hollow degree of precursor will promote the degree of crystallization, which cause the products transform from amorphous to highly crystallized Fe_2O_3, as shown in Fig. 3g.

2.1.2. Applications of Fe_2O_3 derived from PB

With the foregoing discussion, it is learned that the annealed products of PB under aerobic atmosphere are generally Fe_2O_3 with different phases which own large surface areas and hierarchical porous structures. These nanomaterials have been widely used in different areas such as carrying anticancer drugs [52,57] extracting heavy metal ions from waste water [51,59]. In this section, the applications were summarized in the field of energy storage and conversion, including LIBs, lithium sulfur batteries (Li/S batteries), supercapacitors and catalysis [53,60,61].

2.1.2.1. Li-ion batteries. Fe_2O_3 has long been regarded as an ideal anode for LIBs, owning to its high theoretical specific capacity about 1007 mAh g^{-1}. The lithium storage mechanism of Fe_2O_3 is based on the redox reaction mechanism. Upon lithiation, Fe_2O_3 is reduced to metallic Fe nanocrystals and dispersed into Li_2O matrix; during delithiation, Fe nanocrystals reversibly returns back to their initial oxidation states:

$$Fe_2O_3 + 6Li^+ + 6e^- \leftrightarrow 3Li_2O + 2Fe$$

On the one hand, Fe_2O_3 exhibits many advantages such as nontoxicity, high corrosion resistance and low processing cost [62]. On the other hand, however, Fe_2O_3 suffers from poor cycle ability due to the drastic volume change during the charge–discharge processes. Besides, the low conductivity of iron oxides also leads to worse rate performance. Therefore, various nanostructured Fe_2O_3 have been synthesized to solve the above problems [63].

Owing to its unique porous structure, Fe_2O_3 derived from PB as described above exhibits better performance compared to conventionally synthesized Fe_2O_3 when utilized in LIBs. Zhang et al. [45] synthesized PB via a facile solution method in air, and its oxidation products Fe_2O_3 was used as anode in LIBs. The morphology of PB and Fe_2O_3 is shown in Fig. 4a and b. The smooth surfaces of PB became rough after annealing, which meant the porous structures formed on Fe_2O_3. The porous Fe_2O_3 exhibits superior electrochemical performance, which exhibits 800 mAh g^{-1} at 200 mA g^{-1} and 85% of the capacity preserved after 50 cycles (Fig. 4c). This result outperforms conventionally prepared Fe_2O_3 (α-Fe_2O_3), which could only preserve 50% of its initial capacity after same cycle numbers. The porous Fe_2O_3 also exhibits superior rate performance, delivering a stable discharge capacity about 530 mAh g^{-1} at 1500 mA g^{-1} which is also much higher than the ordinary α-Fe_2O_3 (almost no capacity at such a high current density) (Fig. 4d). The remarkable difference of cycling stability and rate capability of these Fe_2O_3 could be attributed to the interconnected nano-sized particles and porous structures. Both the smaller size and porous structure of Fe_2O_3 lead to shorter distance for Li^+ to transfer during charging–discharging processes, which is beneficial to the rate capability. Moreover, the porous structure of Fe_2O_3 nanocubes will offer more void spaces which could buffer the volume variation during cycling and lead to the improvement of cycle stability. To obtain Fe_2O_3 anode with superior performance, various methods such as structure modification, mixing with other metal oxides and carbon coating have been previously used.

2.1.2.1.1. Structure modification. The electrochemical performance of Fe_2O_3 could be further improved by structural design. In order to further enhance the electrochemical performance of iron oxide derived from PB, Zhang et al. [49] introduced hollow structure and porous shell architecture into the iron oxide by raising annealing temperature, as shown in Fig. 4. While annealed at 350 °C, the product exhibits microboxes with smooth surface, which inherited the size and cubic shape of the PB precursor (Fig. 4e). When the annealing temperature increased to 550 °C, the final product Fe_2O_3 exhibited microboxes with highly porous shells (Fig. 4f). After calcination temperature reached 650 °C, the porous shell of the microboxes further evolved into a complex hierarchical structure which consisted of sheet like Fe_2O_3 subunits (Fig. 4g). These unique structures determined the electrochemical performance. As shown in Fig. 4h, the Fe_2O_3 with hierarchical structure exhibits the highest capacity and the best cycling stability, which has reversible capacity of 945 mAh g^{-1} in the 30th cycles at 200 mA g^{-1}. This outstanding electrochemical performance is directly related to the as-designed structure: Both the hollow structure and porous shell architecture facilitated the penetration of electrolyte and transportation of Li^+ ions in the electrode. Such hierarchical hollow structures could efficiently release the stress caused by volume variation upon cycling. Furthermore, the Fe_2O_3 microboxes with high crystallinity and structural stability would also contribute to retaining the pristine nanostructure during cycling.

2.1.2.1.2. Forming compounds with other metal oxides. Although the electrochemical performance of Fe_2O_3 derived from PB could be improved by structural design, its cycling stability still needs to be improved. The composite method can solve this problem in some degree. However, the compound directly mixed by different metal oxides exhibits poor electrochemical performance. Yang et al. [56] synthesized bimetallic organic frameworks by ion exchange of PB, which was annealed to form porous nanocomposites of Fe_2O_3/CuO. The charge transfer resistance of porous Fe_2O_3/CuO composite electrode is lower than that of the simply mixed Fe_2O_3/CuO, which means a better electronic conductivity of Fe_2O_3/CuO composite, as shown in Fig. 4i. The reason lies in the good contact between CuO and Fe_2O_3 in the porous composite, the charge transfer resistance at grain boundaries dramatically decreases. Therefore, excellent electrical conductivity of Fe_2O_3/CuO composite leads to excellent rate performance (Fig. 4j). In addition, the electrochemical performance of the above mixture is much higher than the mechanical mixture of Fe_2O_3 and CuO, which could only achieve to 694 mAh g^{-1} after the same cycles at the same

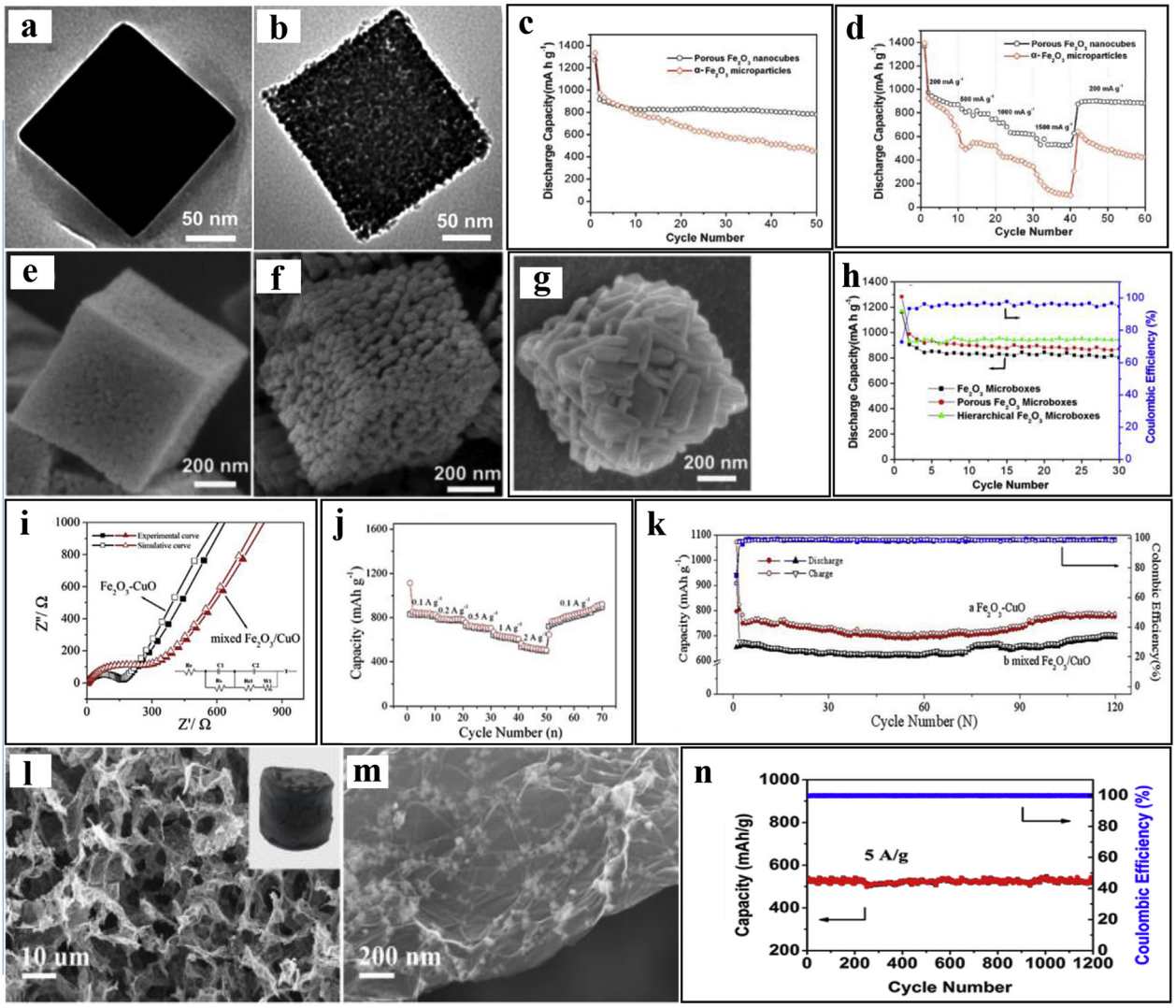

Fig. 4. TEM images of PB precursor (a) and porous Fe_2O_3 nanocubes (b). (c) Cycling stability (current density of 200 mA g^{-1}) and (d) rate performance of porous Fe_2O_3 nanocubes and α-Fe_2O_3 microparticles at the voltage range of 0.05–3 V [45]. FESEM of hollow Fe_2O_3 derived from PB at 350 °C (e), 550 °C (f) and 650 °C (g). (h) Cycling performance of Fe_2O_3 microboxes (350 °C), porous Fe_2O_3 microboxes (550 °C), and hierarchical Fe_2O_3 microboxes (650 °C) and coulombic efficiency of porous Fe_2O_3 microboxes (550 °C) at the current density of 200 mA g^{-1} [49]. (i) Experimental and simulated nyquist plots of LIBs with as-prepared Fe_2O_3/CuO and physically mixed Fe_2O_3/CuO without charge or discharge at the range of 0.01 Hz to 1000 kHz with an insertion of equivalent circuit. (j) Rate performance of Fe_2O_3/CuO cubes. (k) Cycling performance of porous Fe_2O_3/CuO (curve a) and physically mixed Fe_2O_3/CuO (curve b) when used as anode in LIBs at the current density of 500 mA g^{-1} [56]. (l and m) SEM images of as-prepared 3DG/Fe_2O_3 annealed at 250 °C for 2 h. (n) Cycling stability of 3DG/Fe_2O_3 at a high current density of 5 A g^{-1} [65].

current density, as shown in Fig. 4k. In addition to forming compounds with CuO, Fe_2O_3 derived from PB could be also compounded with other metal oxides. Li et al. [64] synthesized Fe_2O_3/Co_3O_4 from the annealing of $Fe_4[Fe(CN)_6]_3$ and $Co(OH)_2$. Owing to the high conductivity and stabilizing effect of inner Fe_2O_3 layered hollow microcubes, the nanocomposite exhibits superb electrochemical properties, which could obtain a specific capacity of 500 mAh g^{-1} at 100 mA g^{-1} and a high initial coulomb efficiency of 74.4%. Zhang et al. [34] synthesized iron oxide hollow microboxes with hierarchical multi-shelled structures derived from PB and compounded it with other oxides (Sn, Si, Ge, Al, B) through coupling the condensation reactions. It is found that the Fe_2O_3–SnO_2 compound displayed the best electrochemical performance, showing a reversible capacity of 500 mA h g^{-1} for 100 cycles.

Besides, other than the thermal treatment of PB with other precursor and compound with other oxides after obtaining Fe_2O_3 from PB, another effective method to obtain compounds with Fe_2O_3 from PB and other metallic oxide is by thermal treatment of PBA directly, which is easier to implement and less expensive. Chen's group [109] synthesized $Mn_{1.8}Fe_{1.2}O_4$ nanocubes derived from $Mn_3[Fe(CN)_6]_2.nH_2O$ in air, the as-prepared oxide exhibited superb performance in lithium ion batteries by achieving 827 mAh g^{-1} after 60 cycles at the current density of 200 mA g^{-1}. The excellent electrochemical performance could be attributed to the interconnected porous structures, which shorten the diffusion length of Li-ions and buffer the volume expansion during cycling. In addition, Yuan's group [110] synthesized Fe–Co oxide nanocubes by the thermal treatment of PBA. After forming compounds with graphene aerogel, the Fe–Co oxide@GA composite showed excellent performance when used as anode in LIBs, exhibiting 947 mAh g^{-1} at 100 mA g^{-1} after 130 cycles.

2.1.2.1.3. Carbon coating. In consideration of the low electronic conductivity of iron oxide, carbon coating is also an effective approach to improve its electrochemical performance. Jiang et al. [65] designed iron oxide compounded with three-dimensional graphene (3DG), obtained from PB and graphene oxide (GO). The

morphology of as-prepared compounds is shown in Fig. 4l and m, the 3DG/Fe_2O_3 inherited the 3D porous structure of 3DG/PB and the iron oxide nanoparticles also maintained microscopic morphology of PB nanoparticles. However, different from PB nanoparticles, porous nano-frameworks can be identified in the Fe_2O_3 nanoparticles. Owing to the superb ionic and electronic conductivity of three-dimensional graphene, the 3DG/Fe_2O_3 exhibited high capacity (523.5 mAh g^{-1}) at a high current density of 5 A g^{-1}. After 1200 cycles, a capacity retention of 98% was achieved (Fig. 4n). This superb cycling stability is ascribed to the robust graphene shell.

2.1.2.2. Other applications. Except for LIBs, Fe_2O_3 derived from PB can be also used in Li/S batteries, supercapacitors and catalysis. For Li/S batteries, the dissolution of intermediate polysulphide reaction species into electrolyte will lead to the whole system to be unsafe and unstable [66,67]. Zhao et al. [61] synthesized porous Fe_2O_3 nanoparticles derived from PB, and mixed it with sulfur, which was used as cathode for Li/S batteries. The porous Fe_2O_3 acts as an internal polysulfide reservoir and suppresses the shuttle effect.

Metal oxides are known to provide high energy densities in supercapacitor applications, owing to their pseudo-capacitance. Tanaka et al. [54] synthesized a new composite combining graphene oxide (GO) sheets with iron oxide derived from PB nanoparticles. The compound exhibits a high specific capacitance of 91 F g^{-1} at a scan rate of 20 mV s^{-1}, which is higher than pure graphene oxide (81 F g^{-1}) and pure Fe_2O_3 (47 F g^{-1}). The enhanced electrochemical performance of GO/IO (graphene oxide and iron oxide) can be explained by the insertion of IO nanoparticles into GO layers, which provides a well-spaced electrical transportation path for electrolytes and ions and make it easy for electrolytes to soak the whole electrode surface.

As for catalytic field, the Fe_2O_3 derived from PB in air could be utilized in electrocatalytic and photocatalytic applications. Teng et al. [68] designed Fe_2O_3 microboxes derived from PB and loaded on macroporous carbon (MPC), which was used as a sensitive electrochemical sensor for nitrobenzene. The Fe_2O_3/MPC showed a low detection limit, wide linear range, high sensitivity and good stability. Based on PB, Zakaria et al. [41] synthesized Fe_2O_3 with different morphologies, surface areas, and degrees of through changing the annealing time of calcination. When the calcination time is 7 h, the α-Fe_2O_3 exhibited superb performance when used on photocatalytic applications. Besides, the Fe_2O_3 derived from PB could be utilized to contain other catalysts. Tanaka et al. [69] synthesized Fe_2O_3 annealed from PB at different temperatures. 11 wt% of Au nanoparticles can be loaded on Fe_2O_3 cubes without significant aggregation. The Au nanoparticles loaded in Fe_2O_3 exhibited excellent performance when used as the catalysts for CO oxidation owing to the high surface area of iron oxide cubes and the presence of nanoporous structure which not only provided more available sites for adsorption of oxygen molecules but also enhanced the diffusivity of the reactant molecules during the catalytic process.

In summary, the Fe_2O_3 could be obtained through annealing PB in aerobic atmosphere. Upon heating to 300 °C, the crystal water in the lattice can be removed. Around 320 °C, the cyanide fractured and the PB quickly decomposed to amorphous Fe_2O_3. With the continuous temperature rising, the obtained Fe_2O_3 began to crystallize and formed into Fe_2O_3 with different crystal forms. Furthermore, the crystalline structures of the obtained Fe_2O_3 are mainly influenced by annealing temperature, precursor particle size and particle hollowness. Higher annealing temperature, larger particle sizes and hollow degree of precursor will promote the degree of crystallization, causing the products transform from amorphous to highly crystallized Fe_2O_3.

Compared to other method to synthesize Fe_2O_3, the method for obtaining Fe_2O_3 from annealing of PB has a few advantages: (1) The synthesis process of this method is simpler, more repeatable and cost less, which is more suitable for large-scale production. (2) Controllable synthesis of iron oxide with different crystal forms could be realized through this method. (3) Owing to the gas release during annealing, large numbers of pores formed, which will be beneficial in energy storage systems. (4) The morphology of nanocubes could be inherited by the products after annealing, resulting in Fe_2O_3 with special morphologies.

Because Fe_2O_3 derived from PB has large surface areas, large numbers of pores and hierarchical porous structures, superior cycling stability and rate performance are displayed when they are employed as anode in LIBs compared to conventionally prepared iron oxide. Owing to these properties, the obtained Fe_2O_3 could be also utilized in Li/S battery to effectively suppress the shuttle effect. Such materials could also be used in supercapacitors. Generally speaking, this part provides a guidance for obtaining Fe_2O_3 with better performance through structural design from changing synthetic conditions.

2.2. Products obtained in inert atmosphere and their applications

2.2.1. Various products in inert atmosphere

Different from annealing at aerobic atmosphere, the products annealed at inert atmosphere always contain C and N element, for the reason that after the cyanogens fracture, C and N element could not escape in the form of gases and finally remain in the products. Barman et al. [70] have first studied the decomposition of ferricyanide in vacuum. Subsequently, the decomposition products of PB at different temperatures under inert atmosphere were studied clearly. Aparicio et al. [71,72] studied the whole process of PB thermal decomposition under inert atmosphere and explored the decomposition products at different temperatures through TGA, DSC, EGA, TG, XRD and quantitative analysis, as shown in Fig. 5a–d. When the temperature is lower than 300 °C, PB starts to lose its crystalline water without significant structure changes:

$$Fe_4[Fe(CN)_6]_3.5H_2O \rightarrow Fe_4[Fe(CN)_6]_3 + 5H_2O$$

As the temperature increases above 300 °C, the cyanide skeletons of PB begin to collapse and phase transformations occur, followed by continuous carbon nitrides release and formation of porous structures:

$$Fe_4[Fe(CN)_6]_3 \rightarrow 7/3Fe_2[Fe(CN)_6] + 2(CN)_2$$

The phase transformation is completed when the temperature rises to 420 °C. In this process, carbon nitrides continuously decompose and release in the form of gas fragments ($C_2N_2^+$, $C_3N_2^+$, $C_3N_3^+$) [70]. With higher temperatures, the dissociated Fe after skeleton fracture will combine with C to form iron carbon compounds in form of Fe_2C and $Fe_{2+x}C$. (420–580 °C) Fe_2C and $Fe_{2+x}C$ will transform into Fe_7C_3 and C with the increase of temperature, until the temperature reach to 660 °C. From 660 °C to 760 °C, Fe_2C has completely decomposed to Fe_7C_3, Fe_5C_2, Fe_3C, and C. When the temperature reaches to 800 °C, Fe_7C_3 and Fe_5C_2 gradually decompose to Fe_3C and C. Above 800 °C, Fe_3C will decompose to γ-Fe and C. Therefore, the general equation of PB decomposition in inert atmosphere could be described as:

$$Fe_4[Fe(CN)_6]_3.xH_2O \rightarrow 2Fe_3C + Fe + 2C + 7(CN)_2 + 2N_2 + xH_2O$$

The factors affecting the decomposition products of PB under inert atmosphere include annealing temperature, atmosphere, particle size, precursor morphology and heating rate. Among these factors, the annealing temperature and atmosphere are more

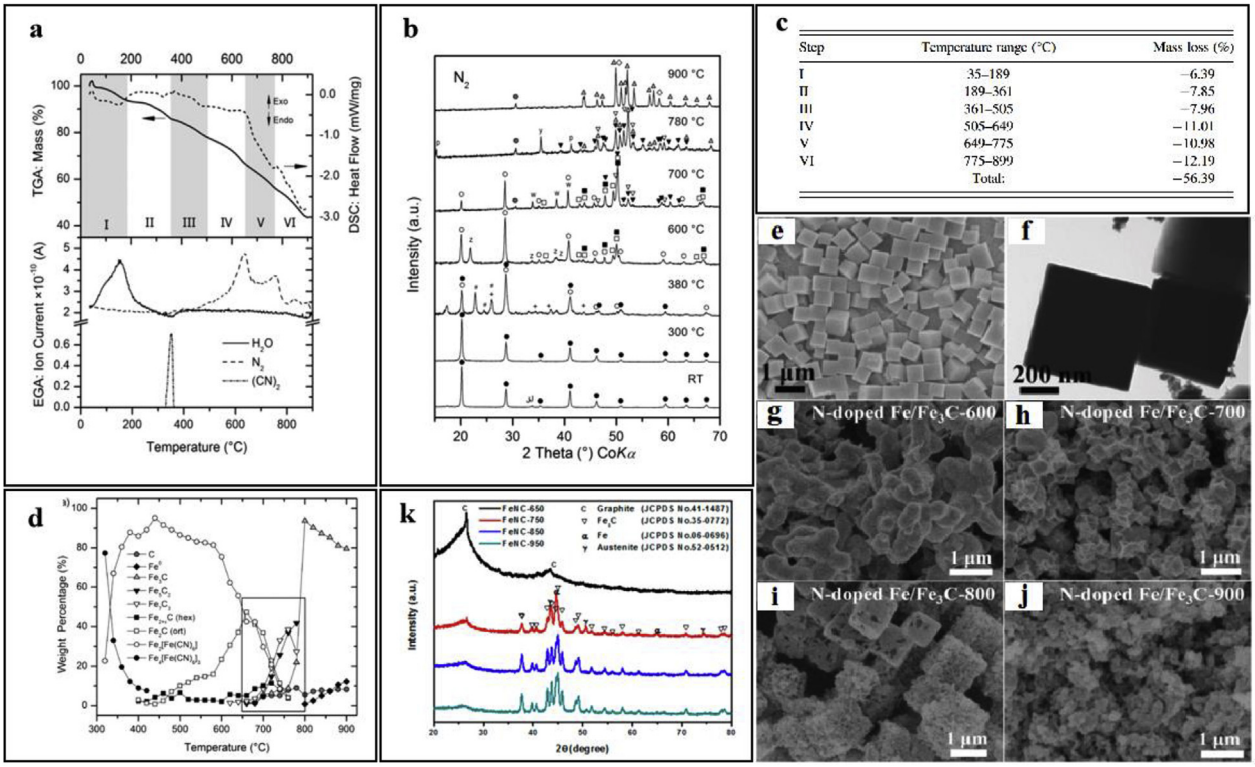

Fig. 5. (a) TGA, DSC and EGA of PB under argon with a heating rate of 5 K min^{-1}. (b) In situ XRD pattern of thermal decomposition of PB under nitrogen. (c) Mass loss of PB from 35 °C to 900 °C in air estimated from TG curve. (d) Quantitative result of the Rietveld analysis of in situ XRD [72]. (e) SEM and (f) TEM image of as-prepared PB microcubes. (g, h, i, and j) SEM images of Fe/Fe_3C@N-doped C by thermal decomposition of PB at 600 °C, 700 °C, 800 °C and 900 °C [80]. (k) XRD patterns of the thermal decomposition products of PB and glucose respectively at 650, 750, 850 and 950 °C [46].

important than others [72]. For easy comparing, recent works of the thermal decomposition of PB at different temperatures in inert atmosphere are summarized in Table 2. From Table 2, it can be concluded that the annealing products of PB under inert atmosphere are directly related to the annealing temperature: when the temperature is lower than 650 °C, the product is Fe_2O_3@N-doped C [73,74]; the product tend to become Fe/Fe_3C@N-doped C when the temperature is above 650 °C [75,76], which can be attributed to the different bonding abilities of Fe—C at different temperatures. Moreover, iron species will catalyze graphitization at low temperatures, forming graphene [74], which exhibits weak bonding with Fe. Therefore, after cooling, the air is easy to enter the product and oxidizes Fe to form Fe_2O_3, however, with higher temperature and longer annealing time, iron and carbon will combine more closely and the air is hard to penetrate into the tightly packed iron and carbon compounds, so Fe/Fe_3C exist in the final thermal decomposition products [77].

Besides, the morphology and nitrogen content of the obtained products will also vary with the annealing temperature. Wen et al. [80] synthesized PB nanocubes through hydrothermal method, as shown in Fig. 5e and f. The as-prepared PB was coated by preformed polydopamine (PDA) and preheated for 2 h at 400 °C, then calcined at 600 °C, 700 °C, 800 °C and 900 °C, respectively. The morphologies of the final products are shown in Fig. 5g–j. At 700 °C, the final product is Fe/Fe_3C@N-doped C with nanocube structures (Fig. 5h); by elevating the temperature to 800 °C, more porous structures can be found in the final product (Fig. 5i); when the temperature reaches to 900 °C, the collapsed structure indicates that the nanocube structure can no longer be maintained (Fig. 5j). In addition, the nitrogen content will decrease as the annealing temperature increasing [39], which is due to the accelerated release of carbon nitride in the form of gas fragments ($C_2N_2^+$, $C_3N_2^+$, $C_3N_3^+$) [58]. Therefore, elevated temperature will cause irregular morphologies and lower nitrogen contents.

Different inert gas will also cause the difference of final products. It has been reported that by sintering PB-glucose mixture at 950 °C under the mixed atmosphere (Ar:H_2 = 95:5), the final product becomes γ-Fe_2O_3@N-doped C rather than Fe/Fe_3C@N-doped C (which usually formed above 650 °C under Ar atmosphere) [60]. Considering the products are mainly decided by the combination degree of Fe and C, we guess this may be due to the presence of reducing atmosphere inhibits the combination of Fe and C in a certain degree, which causes the product oxidized in the air.

Table 2
The works of thermal decomposition of PB under alert atmosphere in recent years.

Temperature	Precursor	Product	Atmosphere	Refs.
600 °C	PB/Resorcinol/formaldehyde	Fe_2O_3@N-doped C	N_2	[74]
600 °C	PB/GO/PPy	Fe_2O_3@N-doped C	N_2	[73]
650 °C	PB/Glucose	Fe_2O_3@N-doped C	Ar	[78]
800 °C	PB/GO	Fe/Fe_3C@N-doped C	Ar	[75]
800 °C	PB/GO	Fe/Fe_3C@N-doped C	Ar	[76]
950 °C	PB/glucose	γ-Fe_2O_3@N-doped C	Ar/H_2	[79]

In summary, under inert atmosphere, PB is normally sintered with other organics in order to obtain carbon-containing final products. The products derived from PB and organics under inert atmosphere are mainly dictated by temperature and atmosphere. At low temperature under Ar or nitrogen atmosphere, the degree of infiltration of iron and carbon is low and the carbon layers are loose owing to low degree of graphitization. During cooling process, iron and carbon will separate from each other. Therefore, when the products are exposed to the air, the iron will be oxidized to iron oxide and the final product is Fe_2O_3@N-doped C. Nevertheless, when the temperature is high, the iron will penetrate into the carbon layers, resulting in dense carbon layers with high degree of graphitization, which further prevents the contact between air and Fe during the cooling process. As a result, the final products are generally Fe/Fe_3C@N-doped C. In addition to temperature, the atmosphere will also affect the final products. For instance, the addition of reducing gas (H_2) could also result in products with different compositions. This might be an interesting area to explore in the future.

2.2.2. Final products obtained after acid-washing

In order to better utilize the porous hollow structure of PB, the final products treated under inert atmosphere can be washed with acid. As shown in Table 3, by acid-washing the products annealed at higher temperature (above 700 °C) and lower temperatures, final products with vastly different compositions can be obtained. Yang et al. [46] heated PB-glucose mixture at 650–950 °C under Ar atmosphere. After annealing, the product was washed with concentrated sulfuric acid for 12 h. As shown in Fig. 5k, the product heated at 650 °C exhibits carbon structure after washing; however, when heated at 750 °C, the final product is Fe/Fe_3C@N-doped C, which is similar to the product before acid treatment. The difference origins from the weak bonding energy of Fe–C bond that formed at 650 °C, so the primary product is oxidized to Fe_2O_3 upon the exposure to air, which can be washed away by acid. When the temperature is higher than 750 °C, Fe and C will closely combine to form Fe_3C, which is relatively stable towards oxygen and acids.

To conclude, the products derived from PB and after acid etching are mainly decided by the compositions of sintered products before acid etching, which also rely on the temperature to a large degree. At low temperature, the obtained iron oxide will be washed out thus the final product is N-doped C; for products obtained under high temperatures, the resulted Fe_3C as well as the dense carbon layers are relatively stable in acidic environment, which causes the uncharged products (Fe/Fe_3C@N-doped C) after acid etching.

2.2.3. Applications of the products derived from PB in inert atmosphere

As summarized above, the final products of PB annealed under inert atmosphere could be divided into three categories: Fe_2O_3@N-doped C, Fe–N-doped C and N-doped C. These products could be utilized in LIBs, SIBs, Li/S batteries supercapacitor and catalysis.

Table 3
The works of thermal decomposition of PB under alert atmosphere then treated with acid in recent years.

Temperature	Precursor	Product	Atmosphere	Refs.
550 °C	PB + glucose	N-doped C	Ar	[81]
650 °C	PB + glucose	N-doped C	Ar	[82]
650 °C	PB + glucose	N-doped C	Ar	[83]
700 °C	PB + GO	Fe_xC_y @N-doped C	Ar	[84]
750 °C	PB	Fe/Fe_3C@N-doped C	Vacuum	[70]
800 °C	PB + PFA	Fe/Fe_3C@N-doped C	Ar	[44]
750–950 °C	PB + glucose	Fe/Fe_3C@N-doped C	Ar	[46]
1050 °C	PB	Fe/Fe_3C@N-doped C	Vacuum	[70]

2.2.3.1. Applications of Fe_2O_3@N-doped C.

As a negative electrode in LIBs, the main issues for Fe_2O_3 should be the severe volume expansion and the poor electrical conductivity. Constructing hollow structure and interface coating are effective ways to solve this problem. To achieve this goal, PB mixed with organics could transform to hollow iron oxides with carbon coating after annealing. Therefore, an increasing number of reports on metal oxide/carbon composites derived from PB/organics have been reported in LIBs since 2010 [85].

Pan and co-workers annealed the mixture of PB and glucose at 650 °C and 950 °C in Ar and Ar/H_2 (95:5), the products were hollow polycrystalline γ-Fe_2O_3@graphene and monocrystal γ-Fe_2O_3@graphene, respectively [78,79]. At 650 °C, the Fe_2O_3@graphene composite with core-shell structure was formed, as shown in Fig. 6a and b. The Fe_2O_3 derived from PB was coated with graphene, which came from glucose and experienced a catalytic process during the increase of temperature. The nano-hollow γ-Fe_2O_3@graphene shows high rate performance with an average discharge capacity of 1095, 1072, 1022, 974, 902, 704, and 504 mAh g^{-1} at the rate of 0.1, 0.2, 0.5, 1, 2, 5, and 10 C, respectively. The excellent rate performance benefits from the stability structure, attributed by the hollow structure of γ-Fe_2O_3 and the graphene layer, moreover the graphene layer also provides high electrical conductivity. The product annealed at 950 °C in Ar/H_2 exhibits monocrystal γ-Fe_2O_3@graphene, which is different from the product annealed at 650 °C. Additionally, Fe lattice was detected between γ-Fe_2O_3 and graphene, as shown in Fig. 6c. Interestingly, the monocrystal γ-Fe_2O_3@graphene exhibits better cycling stability compared with the hollow polycrystalline γ-Fe_2O_3@graphene. The superior electrochemical performance of monocrystal γ-Fe_2O_3@graphene comes from the higher graphitization degree and quality layers of graphene, which offer conductive network and buffer the volume changes during the electrochemical process.

Other than Fe_2O_3, Fe_3O_4 derived from PB coating with carbon reduced from other organics have been chosen as anode in LIBs. Chen et al. [86] obtained carbon-covered Fe_3O_4 hollow cubic hierarchical porous composite through calcining PB and resorcinolformaldehyde (RF) resin. The products are found to have a strong dependence on annealing temperature. The morphologies of the annealed products are presented in Fig. 6d–f, where porous structure gradually formed as the temperature increased. As shown in Fig. 6g, different phase structures are formed at different temperatures, including amorphous, Fe_3O_4 and Fe at 400 °C (Fe_xC400), 600 °C (Fe_xC600) and 800 °C (Fe_xC800), respectively. In addition, different products demonstrate different electrochemical properties. As shown in Fig. 6h and i, the Fe_3O_4/C (Fe_xC600) exhibits the best electrochemical performance. Although its discharge capacity faded in the initial dozen cycles, it then almost recovered to that of the first cycle, which was close to 1100 mAh g^{-1}, higher than the theoretical capacity of Fe_2O_3 (1007 mAh g^{-1}). This result might be attributed to the synergistic effect between Fe_3O_4 and carbon material, or the lithium storage behaviour on the interface. Compared with Fe_xC400 and Fe_xC800, Fe_xC600 also showed better rate performance of 500 mAh g^{-1} at the current density of 500 mA g^{-1}. The electrochemical performance of Fe_3O_4 derived from PB could be further promoted through coating with double-layer carbon [87]. The Fe_3O_4 (derived from PB after thermal treatment) was second annealed with PDA at N_2 atmosphere. The obtained Fe_3O_4/AC (amorphous carbon) were then compounded with rGO (reduced graphene oxide) through a well-designed self-assembly method. Consequently, a 3D constructed rGO/Fe_3O_4/AC was built with double-layer carbon. Owing to the excellent conductivity and the function of buffering mechanical stress of double-layer carbon, the rGO/Fe_3O_4/AC exhibited superb electrochemical performance, which outperformed pure Fe_3O_4 and Fe_3O_4 with monolayer carbon (Fe_3O_4/AC and Fe_3O_4/rGO).

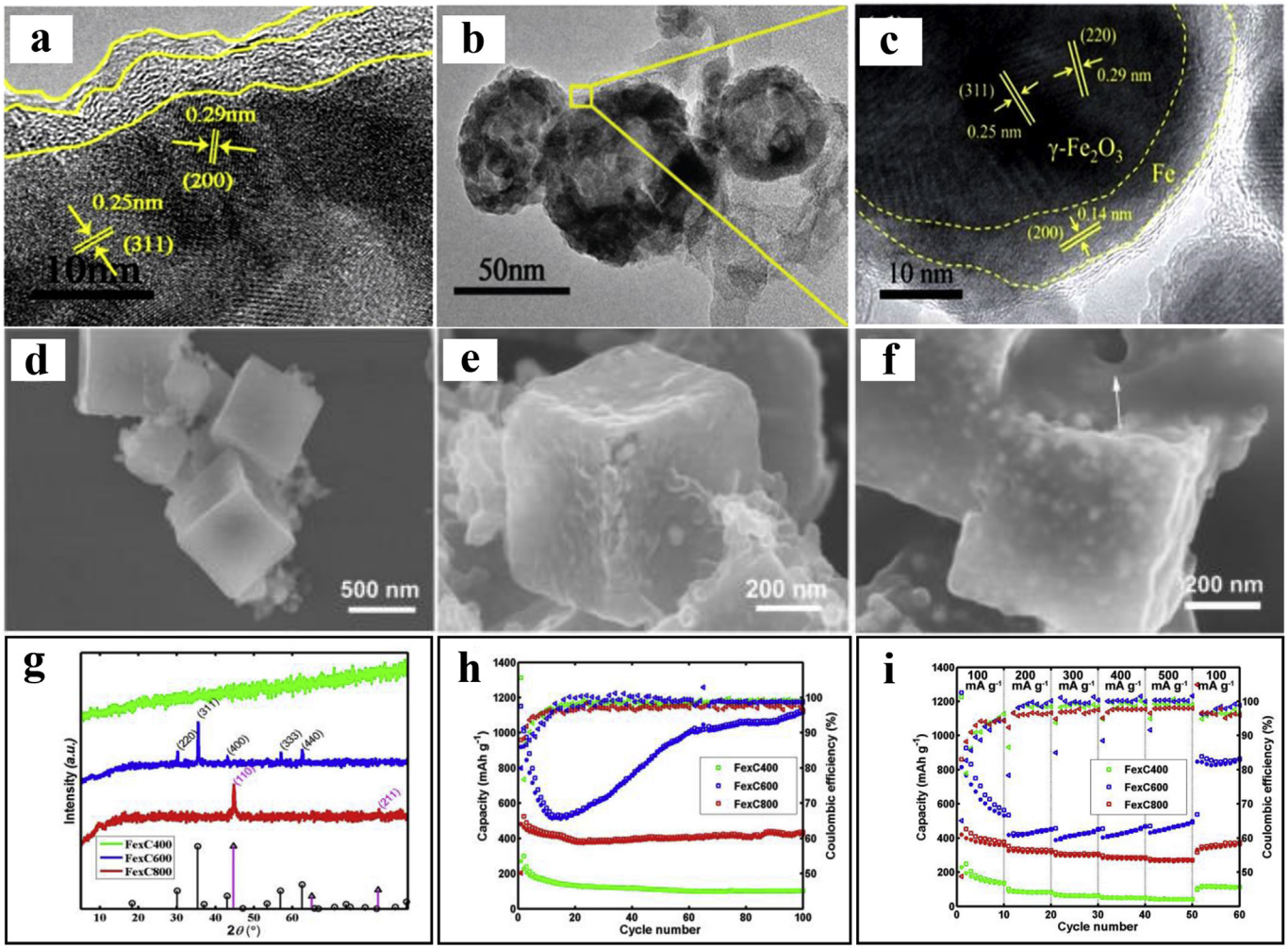

Fig. 6. (a) and (b) HRTEM image of hollow polycrystalline γ-Fe_2O_3@graphene [78]. (c) HRTEM image of monocrystal γ-Fe_2O_3@graphene [79]. (d)–(f) FESEM images of the products derived from PB@RF respectively at 400 °C (d), 600 °C (e) and 800 °C (f). (g) XRD patterns of as-prepared Fe_xC400, Fe_xC600 and Fe_xC800. (h) Charge–discharge cycle curves (at the current of 100 mA g^{-1}) and (i) rate performance of Fe_xC400, Fe_xC600 and Fe_xC800 when used as anode of LIBs [86].

Fe_2O_3@N-doped C could be also utilized in Li/S batteries. Compared to ordinary FeS_2 derived from Fe_2O_3 (annealed by PB) and S, FeS_2 derived from Fe_2O_3@N-doped C has better electrochemical performance. Liu et al. [88] synthesized yolk-shell FeS_2@carbon (FeS_2@C) spheres through annealing of PB and RF at Ar atmosphere. Owing to the unique yolk-shell structure, the FeS_2@C effectively prevented the volume expansion and dissolution of the active materials when used as anodes in LIBs. The FeS_2@C electrode exhibited superb electrochemical performance which could achieve 560 mAh g^{-1} at the current density of 100 mA g^{-1} for 100 cycles. Pan and co-workers [89] synthesized porous Fe_2O_3@N-doped C derived from PB and glucose, and mixed it with sulfur. When used as cathode for Li/S batteries, the FeS_2@N-doped C has a superior electrochemical performance with a high reversible capacity of 484.7 mAh g^{-1} at 0.5 A g^{-1} corresponding to a specific capacity of 713.49 Wh kg^{-1} and a fast recharging performance of 281.4 mAh g^{-1} at 5 A g^{-1} at room temperature. This superior performance can be attributed to the short Li-ionic diffusion distance of FeS_2, which provided by the N-graphene shell [90]. The N-graphene shell also enhanced the structure stability and decreased the shuttle effect of sulfur. In addition, the products derived from PB under inert atmosphere have also been employed in supercapacitor and catalysis applications [91–93].

2.2.3.2. Applications of Fe/Fe_3C@N-doped C. As discussed above, the carbon layers become denser when annealed at higher temperature, which could prevent air entering the carbon layers and prevented Fe oxidized to iron oxide, so iron and carbon will permeate to each other and formed Fe/Fe_3C@N-doped C. In order to obtain ideal core-shell structure of carbon, PB was always mixed with different carbon sources [84]. The as prepared products from PB, PB/C or PB/organics has a broad application field, such as extracting uranium from nuclear waste [80] and oxidase-mimic activity [94]. As for energy storage field, the Fe/Fe_3C@N-doped C are mainly used for catalysis [95].

The catalyst of oxygen reduction reaction (ORR) plays an important role in the industrial application of fuel cells. The ORR behaviours are decided by the intrinsic properties of catalyst associated with the type and the number of catalytic active sites, specific surface area, conductivity and mass transport in catalyst layer [84]. Pt and its alloys, owing to their high catalytic efficiency, have been widely used for oxygen reduction reaction. Synthesizing nano-composites derived from noble metals doped PB or PBA through thermal treatment is an effective method for tuning or enhancing the catalytic activity of noble metals. Chen's group synthesized a few nanoalloys (including Pt, Ru, Pd, Ir etc) derived from noble metals doped PB and PBA, which realized the regulation

and optimization of the performance on electrocatalytic hydrogen evolution [117–120]. However, considering its high cost, low abundance, weak durability, crossover effect and CO poisoning [96], it is necessary to find another catalysis materials, which could not only have high catalytic efficiency, but also has a low cost. Fe–N-based carbon catalysts have attracted considerable attention as one of the most promising candidates owing to their low cost and high catalytic activity brought about by nitrogen incorporation and Fe-coordinated nitrogen species [97]. Cui's group [84] synthesized iron carbide nanoparticles supported on highly nitrogen-doped 3D porous carbons from PB/graphene oxide composite (GO) under Ar atmosphere. The as-prepared sample exhibited superb catalytic activity, superior durability and methanol tolerance for ORR in both acidic and alkaline media. Chen et al. [98] obtained a Fe–N co-doped carbon by the annealing of polyaniline-Prussian blue composite (PANI-PB). The as prepared Fe–N co-doped carbon exhibits excellent catalytic properties, when catalysts in O_2-saturated 0.1 M KOH solution, the composite catalyst exhibits a high positive cathode peak. Liu et al. [76] prepared Fe/Fe_3C@N-doped C by annealing the mixture of PB and GO, the product displayed outstanding catalytic activity in the ORR on par with the state-of-the-art Pt/C catalyst at the same mass loading in alkaline media.

Hou et al. [75] prepared N-doped Fe/Fe_3C@C/RGO through annealing the mixture of PB and GO, as shown in Fig. 7a and b. To further explore the contribution to catalytic efficiency of N doping, RGO and Fe_3C, the RGO, N-doped Fe/Fe_3C@C, N-doped Fe/Fe_3C@C-RGO (the N-doped Fe/Fe_3C@C/RGO with ex-situ synthesized), N-doped Fe/Fe_3C@C/RGO and the etched N-doped Fe/Fe_3C@C/RGO were tested at a rotation rate of 1600 rpm in O_2-saturated 0.1 M KOH solution, as shown in Fig. 7c and d. Remarkably, N-doped Fe/Fe_3C@C/RGO exhibits higher positive ORR onset potential (1 V) and half-wave potential (0.93 V) than N-doped Fe/Fe_3C@C. The superior performance comes from NRGO sheets, which serve as a conduction path for electrons and act as an active site for ORR. In order to explore the effect of N-doping in NRGO sheets, the author synthesized the hybrid material (N-doped Fe/Fe_3C@C-RGO) and tested its ORR activity at the same condition. Compared with N-doped Fe/Fe_3C@C-RGO, N-doped Fe/Fe_3C@C/RGO the exhibits higher onset potential and half-wave potential, which could be attributed to the increase of active sites provided by the N-doping in RGO sheets. To further clarify the roles of Fe and Fe_3C in ORR, etched N-doped Fe/Fe_3C@C/RGO was used as the comparison group, which exhibited a more negative onset potential and a much smaller current density. Therefore, it is confirmed that Fe/Fe_3C nanoparticles could improve the catalytic performance for ORR.

Non-precious metal catalysts for oxygen reduction reaction (ORR) are widely utilized in anion exchange membrane fuel cells (AEMFCs) owing to their high stability and low cost. Hu et al. [111] synthesized a novel Fe_3C-based spherical catalyst, which exhibited superb activity and durability in both Nafion-based low temperature and acid doped polybenzimidazole-based high temperature proton exchange membrane fuel cells. Huang et al. [99] synthesized nanostructured Fe_3C/FeS encapsulated carbon (FeCN-S) derived from pyrolyzed poly (3,4-ethylene dioxy thiophene) hydrate (PEDOT) and Prussian blue (PB). The PEDOT and PB are heated at 600 °C (FeCN-S-600) 800 °C (FeCN-S-800) and 1000 °C (FeCN-S-1000), respectively. The morphologies of products are shown in Fig. 7e–g. At 800 °C, porous structures began to form. However, with the continuous increase of temperature, the nanocubes started to aggregate. (FeCN-S-1000) Therefore, the catalyst annealed at 800 °C (FeCN-S-800) presented the highest disk current (*Id)* and lowest ring current (*Ir),* as shown in Fig. 7h. When utilized in cathode of anion exchange membrane fuel cells (AEMFCs), it exhibited better performance compared to Pt/C. The Pt/C utilized in cathode produces a maximum power density of 142 mW cm^{-2} and FeCN-S-800 produces a maximum power density of 125 mW cm^{-2}. In addition, the durability of FeCN-S-800 in the cathodes of AEMFCs through hydrogen and oxygen has been tested. At 0.5 V, the FeCN-S-800 still retains 87% of initial value, which is much better than Pt/C in cathode.

In addition, another important application of Fe/Fe_3C@N-doped C is used as cathode catalysts in Zn-air batteries. Wang's group [112]

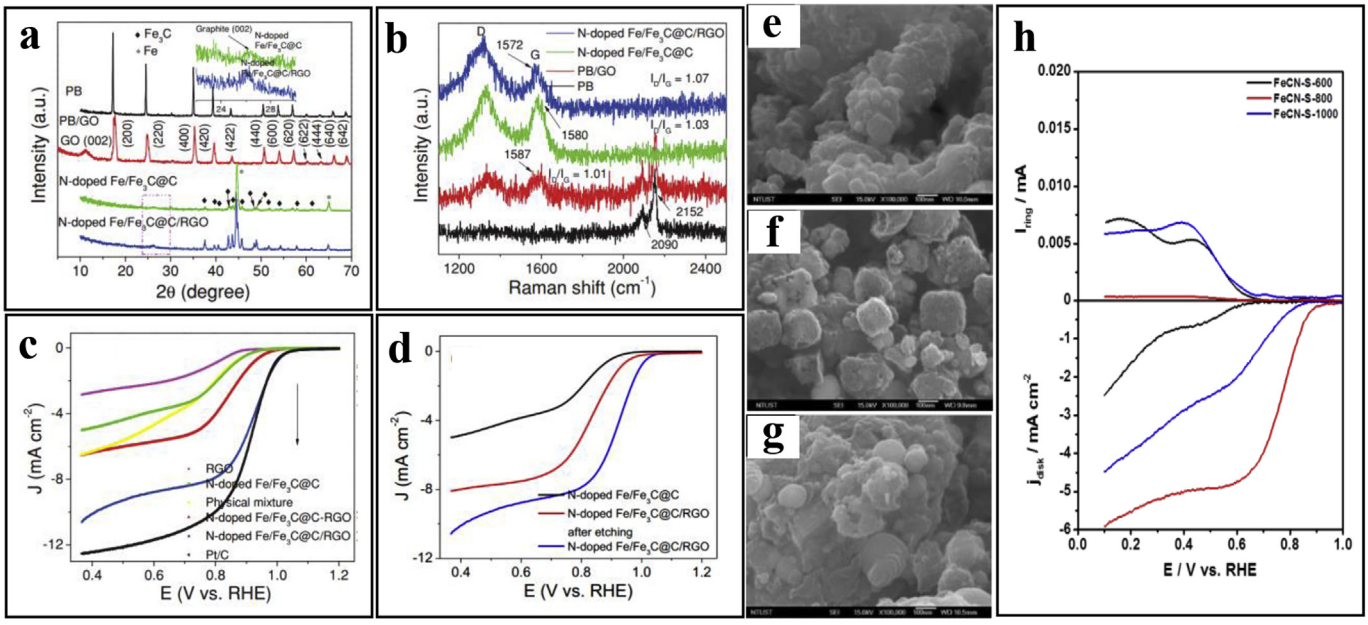

Fig. 7. (a) XRD patterns and (b) Raman spectra of PB, PB/GO, N-doped Fe/Fe_3C@C and N-doped Fe/Fe_3C@C/RGO. (c) LSV curves of RGO, N-doped Fe/Fe_3C@C, physical mixture, N-doped Fe/Fe_3C@C-RGO, N-doped Fe/Fe_3C@C/RGO and Pt/C at a rotation rate of 1600 rpm in O_2-saturated 0.1 M KOH solution. (d) LSV curves of RGO, N-doped Fe/Fe_3C@C after etching and N-doped Fe/Fe_3C@C at a rotation rate of 1600 rpm in O_2-saturated 0.1 M KOH solution [75]. HRSEM images of FeCN-S annealed at different temperatures: (e) 600 °C, (f) 800 °C and (g) 1000 °C. (h) ORR curves of FeCN-S-600, FeCN-S-800, and FeCN-S-1000 [99].

proposed a bifunctional oxygen electrocatalyst (Fe@C-NG/NCNTs) consists of Fe/Fe_3C@C (Fe@C), 3D N-doped graphene and bamboo-like CNTs. Fe@C-NG/NCNTs exhibited a voltage gap increase of only 0.13 V, almost only half of Pt/C + Ir/C (0.22 V). Pan's group [46] synthesized a Fe/Fe_3C wrapped by N-doped graphitic layers by calcining PB and glucose and utilized it as catalyst for Zn-air batteries. When used as catalysts in Zn-Air batteries, it exhibited a maximum power density of 186 mW cm^{-2}, which is slightly higher than Pt/C catalyst.

Moreover, the electrochemical performances of Fe—N compounds derived from PB have been tested in LIBs and Li/S batteries. Che et al. [100] synthesized a nitrogen and sulfur doped carbon with Fe_2C nanocrystals (Fe_2C@C) derived from PB and 3,4-ethoxylene dioxy thiophene (PEDOT) through simultaneous polymerization-precipitation technique and thermal treatment. The Fe_2C@C electrode with core-shell structure exhibited a high specific capacity (657.7 mAh g^{-1}) at the current density of 0.2 A g^{-1} and 509.1 mAh g^{-1} at a high current density (6 A g^{-1}). Su et al. [101] designed Fe_3C@N-GE-CNTs by dehydrated $Na_4Fe(CN)_6$ annealed under N_2 atmosphere. Sulfur is impregnated into the as-prepared Fe_3C@N-GE—CNTs through melt-diffusion strategy. As a result, the cathode exhibited a high reversible capacity (1221 mAh g^{-1}) at 0.2 C and superb rate performance (220 mAh g^{-1} at 10 C).

2.2.3.3. Applications of N-doped C. Loose carbon layers are formed at low temperature, so the Fe_2O_3 or Fe_3C in the final products could be washed away by acid, forming N-doped carbon. The obtained N-doped C could be utilized in supercapacitors and SIBs.

Carbon-based materials are considered as one of the most suitable materials for supercapacitors, owing to its high conductivity, stability in different environments, large specific surface area, and a large variety of carbon-rich precursors [102]. Wickramaratne et al. [74] prepared graphitic mesoporous carbons derived from polyvinylpyrrolidone (PVP)-coated PB at nitrogen atmosphere. Owing to the catalytic graphitization of iron species, the carbon with different degrees of graphitization can be obtained with different stoichiometric ratios and annealing temperatures. The as-prepared carbons exhibited outstanding performance on double layer capacitors owing to their special porous structures, which achieved a large capacitance of 211 F g^{-1} in 1 M H_2SO_4 electrolyte. In order to achieve higher pseudocapacitance, N is chosen as a dopant into the carbon [103]. However, N-doping results in lower conductivity and therefore affects the rate performance. To solve this problem, Pan and co-workers [83] has mixed N-doped C with different content of nitrogen, which exhibited high pseudocapacitance as well as superb rate performance. The hollow N-doped C was synthesized through washing annealed products at 650 °C with sulfuric acid. (CS-650) In order to change the content of nitrogen, two products were respectively annealed at 850 °C (CS-850) and 1050 °C (CS-1050), as shown in Fig. 8a—c.

The products annealed at different temperatures exhibited hollow carbon structure and the content of N decreased with the temperature. As shown in Fig. 8d, CS-650 exhibited high specific capacitance at low current density. However, the capacitance dropped sharply as the current density increased. Therefore, the CS-650 was mixed with CS-1050 and the electrochemical performance of mixture was investigated at the same condition. Consequently, the mixture showed excellent rate performance, which is better than CS-650 and CS-1050.

In addition, carbonaceous materials are also regarded as the most promising anode candidate for SIBs. However, the commercial graphite could only exhibit no more than 35 mAh g^{-1} when used as anode in SIBs [104]. Amorphous carbon has superior capacity, but the initial coulombic efficiency is low owing to the high specific surface area. To solve this problem, Pan and co-workers [105] has synthesized N-doped C derived from the mixture of PB and glucose respectively from 550 °C (NC-550) and 660 °C (NC-650) (shown in Fig. 8e and f). The as-prepared products exhibit a wide peak around 26°, corresponding to the (002) face of carbon. Interestingly, the NC-550 shows a much lower specific surface area of 12.1 m^2 g^{-1} compared to NC-650 exhibits a high specific surface area of 553.2 m^2 g^{-1} (Fig. 8g). The lower specific surface area reduces the side reaction on interface, promoting the initial coulombic efficiency of 64.9%, which much larger than NC-650. The NC-550 also exhibits outstanding rate performance during charge—discharge processes, which could reach to 212 mAh g^{-1} at a high current density of 500 mA g^{-1} (Fig. 8h). The superb electrochemical performance could be attributed to its unique structure. Both the doped nitrogen and the expanded layer distance facilitate sodium ions storage during the process of charge—discharge, leading to a high capacity. The low specific surface area also reduced the side reaction on interface; hence a high initial coulombic efficiency can be obtained. Instead of being used as anode materials, porous carbon derived from PB could be also utilized as a conductive layer for other anodes in SIBs. Lim et al. [106] designed nitrogen doped 3D porous carbon derived from PB (NC) and then compounded it with WS_2 through solvothermal methods followed by a post annealing process. Owing to the well-defined, nano-structured hierarchical scaffolding and highly conductive nature of the 3D porous carbon framework, the WS_2@NC electrode displayed outstanding performance in LIBs.

In order to mitigate the “shuttle effect” of lithium polysulfide species and improve the conductivity, carbon-based materials have been widely used in Li/S batteries [107]. However, the combination of carbon and polysulfide is weak which could not inhibit the polysulfides shuttling between electrodes. In addition, ordinary carbon structure cannot effectively suppress volume expansion during charging and discharging. Pan and co-workers [81] has synthesized a pomegranate-like structure N-doped carbon self-assembled with nano-hollows through thermal treatment of PB and glucose. The structure is composed of smaller hollows with thinner N-doped graphene shells, which are fully embedded in lager hollows with thicker N-graphene-shells. The sulfur is filled into the pores, which are encapsulated by the thin layer graphene shells. With a high areal sulfur loading of 10.1 mg/cm^{-2}, the cathode exhibited superb electrochemical performance owing to that the hierarchal nano-hollows with graphene-shells built a 3D-electronic conduction network and increased the wettability of electrolyte to enhance the Li-ion transport, hence a superb rate performance. Besides, N elements in graphene-shells increased the bonding between polysulfide and carbon, which prevented shuttle-effect effectively, leading to the superior cycling stability.

Last but not least, the N-doped porous carbon derived from PB could be utilized in catalysis. Liang et al. [44] synthesized nitrogen-doped porous carbon through annealing of PB and furfuryl alcohol (FA) after acid etching. The obtained porous carbon exhibited high surface area and displayed excellent electrocatalytic activity and electrochemical stability when used to support Pt nanoparticles as an electrocatalyst for the oxidation of methanol. It is believed that the special structure not only reduces the diffusion rate of carbonaceous species but also leads to more fully oxidation of the carbonaceous species.

In summary, different from the products derived from PB in aerobic atmosphere, the products annealed under inert atmosphere contain C and N element, because C and N cannot combine with oxygen and be released in the form of gas in inert atmosphere. The final products are mostly dictated by the annealing

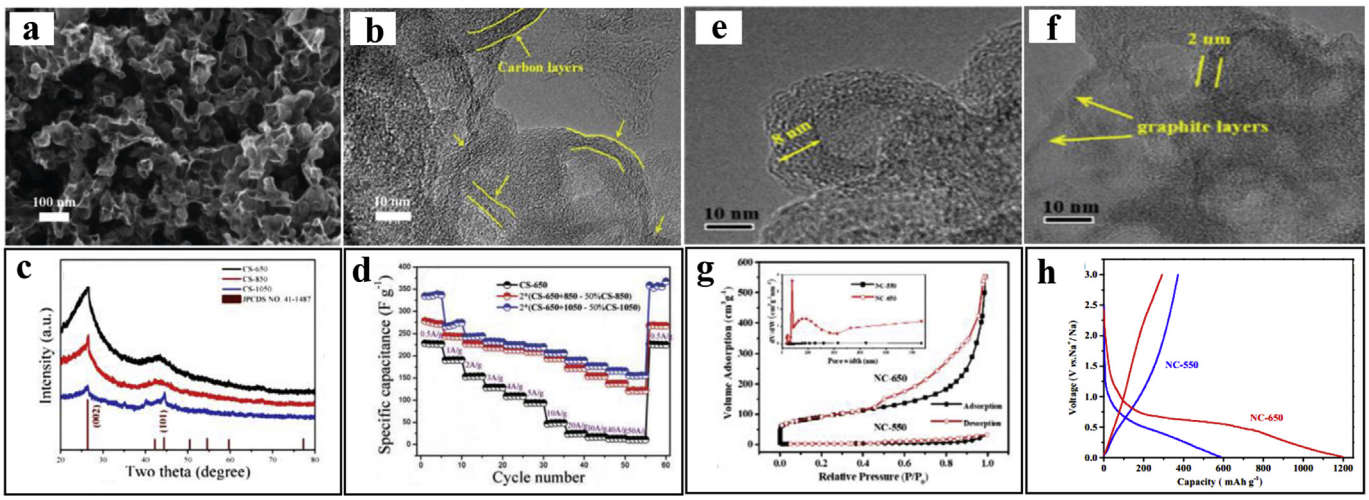

Fig. 8. (a) SEM image and (b) HRTEM image of CS-850. (c) XRD patterns of CS-650, CS-850 and CS-1050. (d) The capacitance retention of CS-650, CS-850, CS-1050, CS-650 + 850 and CS-650 + 1050 at different current densities [83]. (e) and (f) HRTEM images of as prepared products from 550 °C and 650 °C. (g) N_2 adsorption/desorption isotherms of as prepared products from 550 °C and 650 °C. (h) First cycle of capacity-voltage curves of as prepared products from 550 °C and 650 °C [105].

temperature: at low temperatures, the bonding of Fe and C is loose during iron-carbon interpenetration process. Therefore, the carbon layers could not buffer the oxygen and iron atoms will be oxidized when exposed to air. As a result, the final product is Fe_2O_3@N-doped C with core-shell structure; at elevated temperatures, the carbon layers become denser and tightly integrated with Fe, which could prevent Fe from being oxidized, hence Fe/Fe_3C@N-doped C can be obtained. Compared to traditional method to synthesize Fe_2O_3@N-doped C and Fe/Fe_3C@N-doped C, the method for obtaining these products derived from PB in inert atmosphere has a few advantages: (1) The synthesis process of this method is simpler, more repeatable and cost less, which is more suitable for large-scale production. (2) The Fe_2O_3 and Fe/Fe_3C could obtain carbon coating by one step without other steps. (3) The thickness of carbon layers could be partly controlled through controlling the annealing temperature.

To further utilize the unique structure of the products from PB, N-doped C can be prepared by removing Fe_2O_3 from Fe_2O_3@N-doped C through acid treatment. Compared to traditional method to obtain carbon materials, this method has several advantages: (a) It contains Fe that can be one of the most effective catalysts to lower the synthesis temperature of graphene. (b) It can be converted to a nanoporous carbonaceous structure that enhances the performance when utilized in energy storage system. However, because the process of acid etching is not strictly controllable, the reproducibility of final products is still need to be promoted.

Therefore, three different products could be obtained through controlling the temperature of thermal treatment: Fe_2O_3@N-doped C, Fe/Fe_3C@N-doped C and N-doped C. The Fe_2O_3@N-doped C is applied in similar field with Fe_2O_3 derived from PB. Nevertheless, owing to its unique core-shell structure coated with N-doped C, the Fe_2O_3@N-doped C exhibited better performance especially in cyclic stability and rate performance in energy storage field. The Fe/Fe_3C@N-doped C exhibits superior catalytic performance in catalytic field, which could be utilized in fuel cell and Zn-Air batteries. The N-doped C also has a wide application fields such as supercapacitors, SIBs, and Li/S batteries.

3. Conclusion and perspective

This review systematically summarizes the products derived from PB through thermal treatment under different synthesis conditions (as shown in Fig. 9) and their applications in energy storage.

When annealed under aerobic atmosphere, the products are generally Fe_2O_3 with different phases (amorphous, γ, β and α). The crystalline structures of the final products are influenced by annealing temperature, precursor particle size and particle hollowness. Higher annealing temperature, larger particle sizes and hollow degree of precursor will promote the degree of crystallization, which cause the products transform from amorphous to highly crystallized Fe_2O_3. Because Fe_2O_3 derived from PB has large surface areas, large numbers of pores and hierarchical porous structures, superior cycling stability and rate performance are exhibited when they are employed as anode in LIBs compared to conventionally prepared iron oxide. Furthermore, such materials also effectively reduce the shuttle effect when utilized in Li/S battery and provide large pseudo-capacitance when utilized in supercapacitors. There are a few works focused on the application of Fe_2O_3 derived from PB especially in energy storage system, however, they paid little attention to the influence of different crystal structures of Fe_2O_3 on the performance of energy storage devices. As we mentioned above, iron oxides with different structures could be designed using the PB as template with different synthetic conditions. Fe_2O_3 with better performance when used in energy storage system might be obtained from this method. As a result, our work provides guidance for obtaining Fe_2O_3 with better performance through structural design from changing synthetic conditions.

When annealed under inert atmosphere, the products derived from PB are mostly dictated by the annealing temperature: at low temperatures, Fe ions will be oxidized when exposed to air and carbon and nitrogen will not disappear in the form of gas, therefore, the final product is Fe_2O_3@N-doped C with core-shell structure; at elevated temperatures, the carbon layer becomes denser and tightly integrated with Fe, which could prevent Fe from being oxidized, hence Fe/Fe_3C@N-doped C can be obtained. To further utilize the unique structure of the products from PB, N-doped C can be prepared by removing Fe_2O_3 from Fe_2O_3@N-doped C through acid treatment. Therefore, three different products could be obtained through controlling the temperature of thermal treatment: Fe_2O_3@N-doped C, Fe/Fe_3C@N-doped C and N-doped C. The Fe_2O_3@N-doped C is applied in similar field with Fe_2O_3 derived from PB. Nevertheless, owing to its unique core-shell structure

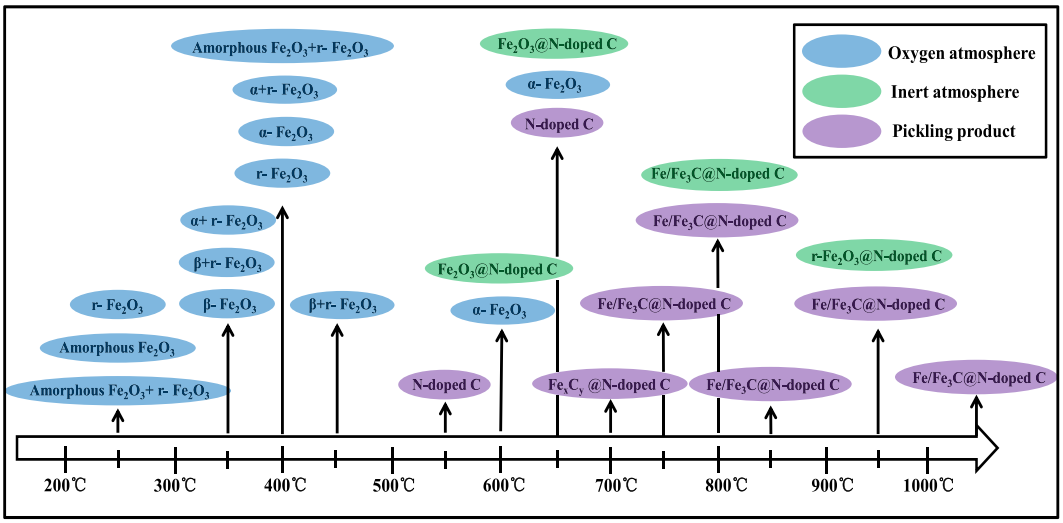

Fig. 9. Summary of calcined products from Prussian blue under different conditions.

coated with N-doped C, the Fe_2O_3@N-doped C exhibited better performance especially in cyclic stability and rate performance in energy storage field. The Fe/Fe_3C@N-doped C exhibits superior catalytic performance in catalytic field, which could be attributed to the synergistic reaction of Fe/Fe_3C, carbon layers and nitrogen doping. The N-doped C also has a wide application field, which could be utilized in supercapacitors, SIBs, and Li/S batteries.

Although the products derived from PB have been widely utilized, it still has potential to become better and new materials derived from PB are still waiting to explore. First, among all products derived from PB mentioned above, only the optimization of Fe_2O_3 derived from PB in LIBs have been reported, which mainly includes structural modification, forming compounds with other metal oxides and coated with carbon. However, optimization techniques for Fe_2O_3@N-doped C, Fe/Fe_3C@N-doped C and N-doped C are rarely reported. The performance of products derived from PB in inert atmosphere could be also promoted by structural modification, element doping and surface modification, as mentioned above in optimization of Fe_2O_3 derived from PB in aerobic atmosphere. For surface modification, SiO_2 capsulation might be a potential choice, which could act synergistically with carbon layers. As we mentioned above, the graphitization degree and the tightness of carbon layers of N-doped C could be promoted through increasing annealing temperature. For Fe_2O_3@N-doped C and Fe/Fe_3C@N-doped C, the denser carbon shells might further promote the cyclic stability when utilized in energy storage systems. For N-doped C, the higher degree of graphitization will possess higher electronic conductivity, which is beneficial for energy storage. For instance, although N-doped carbon exhibits superb coulombic efficiency and capacity as anode materials in SIBs, its electronic conductivity and rate performance still need to be promoted. Through promoting annealing temperature might partly solve this problem.

In addition to optimize the acquired products, it is necessary to explore new materials with better performance. First, iron oxides with different structures could be designed using the PB as template. Although the application of iron oxides derived from PB in different fields has been widely investigated, there are few reports about the structural design of ferric oxide using the PB as template. Besides, the products derived from PB or PBA with noble metal doping always display excellent performance in different researches [113,114]. Therefore, more in-depth study is needed on the products derived from PB or PBA with noble metal doping, which might be a more effective and easier method to synthesize new materials with better performance in many application fields. Furthermore, it has been reported that the graphite/graphene could be catalyzed by transition metals [108]. Therefore, the free Fe released from PB during annealing could catalyze amorphous carbon into graphite/graphene. Based on this principle, carbon materials containing graphite/graphene as well as amorphous carbon can be obtained by synthetic tuning. Moreover, since the catalytic capability of Fe is limited, only amorphous carbon within a certain range could be catalyzed. In this case, the proportion of two different carbon structures could be precisely controlled by tuning the ratios between PB and organics. As a result, our work provides a few methods to obtain products with better performance and design new materials with unique structure using PB as template.

Overall, the research of the products derived from PB through thermal treatment has opened up a promising approach toward high-performance functional nanoporous materials in the field of energy storage and conversion.

Conflicts of interest

There are no conflicts to declare.

Acknowledgements

This work was financially supported by Guangdong Key-lab Project (No. 2017B0303010130), and Shenzhen Science and Technology Research Grant (No. ZDSYS201707281026184).

References

[1] E. Yoo, J. Kim, E. Hosono, H.S. Zhou, T. Kudo, I. Honma, Nano Lett. 8 (2008) 2277–2282.
[2] S.W. Kim, D.H. Seo, X. Ma, G. Ceder, K. Kang, Adv. Energy Mater. 2 (2012) 710–721.
[3] K. Takechi, Y. Kato, Y. Hase, Adv. Mater. 27 (2015) 2501–2506.
[4] L. Peng, Y.Y. Feng, L. Yu, F. Wei, J. Power Sources 220 (2012) 160–168.
[5] F. Jaouen, E. Proietti, M. Lefevre, R. Chenitz, P. Zelenay, Energy Environ. Sci. 4 (2011) 114–130.
[6] A.R. Millward, O.M. Yaghi, J. Am. Chem. Soc. 127 (2005) 17998–17999.
[7] B.B. Panella, M. Hirscher, H. Pütter, U. Müller, Adv. Funct. Mater. 16 (2010) 520–524.
[8] L. Yunling, J.F. Eubank, A.J. Cairns, E. Juergen, K. Victor Ch, L. Ryan, E. Mohamed, Angew. Chem. Int. Ed. 119 (2007) 3342.
[9] V.D. Neff, J. Electrochem. Soc. 132 (1985) 1382–1384.
[10] C.D. Wessells, R.A. Huggins, Y. Cui, Nat. Commun. 2 (2011) 550.

[11] M.G. Nijkamp, J.E.M.J. Raaymakers, A.J.V. Dillen, K.P.D. Jong, Appl. Phys. A Mater. Sci. Process. 72 (2001) 619–623.
[12] N. Stock, S. Biswas, Chem. Rev. 112 (2012) 933.
[13] S. Kitagawa, S. Noro, T. Nakamura, Chem. Commun. 45 (2006) 701–707.
[14] I. Luz, F.X.L.i. Xamena, A. Corma, J. Catal. 276 (2010) 134–140.
[15] L.L. Tan, H. Li, Y. Zhou, Y. Zhang, X. Feng, B. Wang, Y.W. Yang, Small 11 (2015) 3807–3813.
[16] T.T. Li, Y.M. Liu, T. Wang, Y.L. Wu, Y.L. He, R. Yang, S.R. Zheng, Microporous Mesoporous Mater. 272 (2018) 101–108.
[17] G. He, L.F. Nazar, ACS Energy Lett. 2 (2017) 1122.
[18] H. Gang, Z. Feifei, D. Xinchuan, Q. Yuling, Y. Dongming, W. Limin, ACS Nano 9 (2015) 1592–1599.
[19] X. Ge, Z. Li, L. Yin, Nano Energy 32 (2017) 117–124.
[20] R.R. Salunkhe, T. Jing, K. Yuichiro, N. Teruyuki, K. Jung Ho, Y. Yusuke, ACS Nano 9 (2015) 6288–6296.
[21] L. Catala, T. Mallah, Coord. Chem. Rev. 346 (2017) 32.
[22] L. Hu, P. Zhang, Q.W. Chen, J.Y. Mei, N. Yan, RSC Adv. 1 (2011) 1574–1578.
[23] A. Daisuke, C.H. Li, M. Yoshifumi, O. Masashi, Z. Haoshen, D.R. Talham, J. Am. Chem. Soc. 135 (2013) 2793–2799.
[24] Q. Gao, J. Chen, Q. Li, J. Zhang, Z. Zhai, S. Zhang, R. Yu, X. Xing, Inorg. Chem. Front. 5 (2018) 438–445.
[25] P.K. Thallapally, M. Radha Kishan, C.A. Fernandez, M.B. Peter, G.S. Behrooz, Inorg. Chem. 49 (2010) 4909.
[26] Y. Mizuno, M. Okubo, E. Hosono, T. Kudo, K. Oh-Ishi, H. Zhou, J. Phys. Chem. C 117 (2016) 10877–10882.
[27] M. Shokouhimehr, E.S. Soehnlen, J. Hao, M. Griswold, C. Flask, X. Fan, J.P. Basilion, S. Basu, S.D. Huang, J. Mater. Chem. 20 (2010) 5251–5259.
[28] X.Z. Song, L. Qiao, K.M. Sun, Z. Tan, W. Ma, X.L. Kang, F.F. Sun, T. Huang, X.F. Wang, Sens. Actuators B Chem. 256 (2018) 374.
[29] S.H. Lee, Y.D. Huh, Bull. Kor. Chem. Soc. 33 (2012) 874.
[30] J.S. Lee, G. Nam, J. Sun, S. Higashi, H.W. Lee, S. Lee, W. Chen, Y. Cui, J. Cho, Adv. Energy Mater. (2016) 1601052.
[31] R.Y. Wang, C.D. Wessells, R.A. Huggins, Y. Cui, Nano Lett. 13 (2013) 5748–5752.
[32] G. Nyström, A. Marais, E. Karabulut, L. Wågberg, Y. Cui, M.M. Hamedi, Nat. Commun. 6 (2015) 7259.
[33] N. Gang, H. Bo, Q. Li, Z. Ji, H. Bo, C. Zhou, ChemElectroChem 3 (2016) 798–804.
[34] Z. Lei, W.H. Bin, L.X. Wen David, J. Am. Chem. Soc. (2013) 44.
[35] S. Adak, L.L. Daemen, M. Hartl, D. Williams, J. Summerhill, H. Nakotte, J. Solid State Chem. 184 (2011) 2854.
[36] L. Shen, Z.X. Wang, L.Q. Chen, Chemistry 20 (2015) 12559–12562.
[37] P. Nie, L.F. Shen, G. Pang, Y.Y. Zhu, X.G. Zhang, J. Mater. Chem. A 3 (2015) 16590–16597.
[38] Duffort Xiaoqi, Nazar Victor, F. Linda, Adv. Sci. (2016) 1600044.
[39] C. Lee, S.K. Jeong, Electrochim. Acta 265 (2018) 430–436.
[40] B. Kong, J. Tang, Z. Wu, J. Wei, H. Wu, Y. Wang, G. Zheng, D. Zhao, Angew. Chem. Int. Ed. 53 (2014) 2888–2892.
[41] M.B. Zakaria, H. Ming, N. Hayashi, Y. Tsujimoto, S. Ishihara, M. Imura, N. Suzuki, Y.Y. Huang, Y. Sakka, K. Ariga, Eur. J. Inorg. Chem. (2014) 1137–1141.
[42] H. Lin, C. Qianwang, Nanoscale 6 (2014) 1236–1257.
[43] P. Qiling, Z. Haihui, H. Zhenhua, C. Jinhua, K. Yafei, J. Cent. South Univ. Technol. 17 (2010) 683–687.
[44] Y. Liang, J. Wei, X. Zhang, J. Zhang, S.P. Jiang, H. Wang, ChemCatChem 8 (2016) 1901–1904.
[45] L. Zhang, H.B. Wu, R. Xu, X.W. Lou, CrystEngComm 15 (2013) 9332–9335.
[46] J. Yang, J. Hu, M. Weng, R. Tan, L.L. Tian, J. Yang, J. Amine, J.X. Zheng, H. Chen, F. Pan, ACS Appl. Mater. Interf. 9 (2017) 4587.
[47] M. Hu, J.S. Jiang, Y. Zeng, Chem. Commun. 46 (2010) 1133–1135.
[48] G. Zoppellaro, L. Machala, J. Tucek, K. Safarova, Z. Marusak, J. Pechousek, J. Filip, R. Zboril, RSC Adv. 3 (2013) 19591.
[49] L. Zhang, H.B. Wu, S. Madhavi, H.H. Hng, L.X. W Lou, J. Am. Chem. Soc. 134 (2012) 17388–17391.
[50] R. Zboril, L. Machala, M. Mashlan, V. Sharma, Cryst. Growth Des. 4 (2004) 1317–1325.
[51] M. Hu, A.A. Belik, M. Imura, K. Mibu, Y. Tsujimoto, Y. Yamauchi, Chem. Mater. 24 (2012) 2698–2707.
[52] J. Zhou, J. Li, X. Ding, J. Liu, Z. Luo, Y. Liu, Q. Ran, K. Cai, Nanotechnology 26 (2015) 425101.
[53] Z.F. Jiang, D.L. Jiang, A.M. Showkot Hossain, K. Qian, J.M. Xie, Phys. Chem. Chem. Phys. Pccp 17 (2014) 2550–2559.
[54] S. Tanaka, R.R. Salunkhe, Y.V. Kaneti, V. Malgras, M.S.A. Hossain, RSC Adv. 7 (2017) 33994–33999.
[55] M.B. Zakaria, A.A. Belik, C.H. Liu, H.Y. Hsieh, Y.T. Liao, V. Malgras, Y. Yamauchi, K.C. Wu, Chem. Asian J. 10 (2015) 1457–1462.
[56] X. Yang, Y.-B. Tang, X. Huang, H.T. Xue, W.P. Kang, W.Y. Li, T.-W. Ng, C.-S. Lee, J. Power Sources 284 (2015) 109–114.
[57] Q. Mo, J. Wei, K. Jiang, Z. Zhuang, Y. Yan, ACS Sustain. Chem. Eng. 5 (2016) 1476.
[58] M. Hermanek, R. Zboril, Chem. Mater. 20 (2008) 5284–5295.
[59] Y.T. Zhuang, W. Gao, Y.L. Yu, J.H. Wang, Carbon 108 (2016) 190–198.
[60] L. Ling, J. Shi, R. Wang, H. Cao, Z. Liu, J. Alloy Compd. 725 (2017) 544–556.
[61] C. Zhao, S. Cai, F. Xin, Z. Sun, W. Han, Mater. Lett. 137 (2014) 52–55.
[62] C. Jordi, M. Laure, L. Dominique, P. M Rosa, Adv. Mater. 22 (2010) E170.
[63] Z. Wang, L. Zhou, X.W. Lou, Adv. Energy Mater. 24 (2012) 1903–1911.
[64] Z. Li, B. Li, L. Yin, Y. Qi, ACS Appl. Mater. Interf. 6 (2014) 8098.
[65] T. Jiang, F. Bu, X. Feng, I. Shakir, G. Hao, Y. Xu, ACS Nano 11 (2017) 5140–5147.
[66] Y. Diao, K. Xie, S. Xiong, X. Hong, J. Power Sources 235 (2013) 181–186.
[67] J. Xiulei, L. Kyu Tae, L.F. Nazar, Nat. Mater. 8 (2009) 500–506.
[68] Q. Teng, Y. Chen, X. Sun, Y. Wang, L. Fang, W. Lei, J. Zhao, H. Wang, Y. Zhang, J. Alloy Compd. 739 (2018) 425–430.
[69] S. Tanaka, M.B. Zakaria, Y.V. Kaneti, Y. Jikihara, T. Nakayama, M. Zaman, Y. Bando, M.S.A. Hossain, D. Golberg, Y. Yamauchi, ChemistrySelect 3 (2018) 13464–13469.
[70] B.K. Barman, K.K. Nanda, Green Chem. 18 (2016) 427–432.
[71] C. Aparicio, L. Machala, Z. Marusak, J. Therm. Anal. Calorim. 110 (2012) 661–669.
[72] C. Aparicio, J. Filip, L. Machala, Powder Diffr. 32 (2017) 207–212.
[73] T. Yao, J. Zhang, Q. Zuo, H. Wang, J. Wu, X. Zhang, T. Cui, J. Colloid Interf. Sci. 468 (2016) 62–69.
[74] N.P. Wickramaratne, V.S. Perera, B.W. Park, G. Min, G.W. Mcgimpsey, S.D. Huang, M. Jaroniec, Chem. Mater. 25 (2013) 2803–2811.
[75] Y. Hou, T.Z. Huang, Z.H. Wen, S. Mao, S.M. Cui, J.H. Chen, Adv. Energy Mater. 4 (2014) 1220–1225.
[76] Y. Liu, H. Wang, D. Lin, J. Zhao, C. Liu, J. Xie, Y. Cui, Nano Res. 10 (2017) 1213–1222.
[77] Z. Peng, L. Bi, D. Zhang, X. Wang, W. Wei, L. Xiang, Y. Hua, Mater. Res. Bull. 76 (2016) 327–331.
[78] J. Hu, J. Zheng, L. Tian, Y. Duan, L. Lin, S. Cui, P. Hao, T. Liu, G. Hua, X. Wang, Chem. Commun. 51 (2015) 7855.
[79] J. Hu, L. Wen, C. Liu, H. Tang, T. Liu, G. Hua, X. Song, J. Zheng, Y. Liu, Y. Duan, RSC Adv. 6 (2016) 51777–51782.
[80] X.K. Wang, T. Wen, X. Wang, J. Wang, Z. Chen, J. Li, J. Hu, T. Hayat, A. Alsaedi, B. Grambow, Inorg. Chem. Front. 3 (2018).
[81] H. Tang, J. Yang, G. Zhang, C. Liu, H. Wang, Q. Zhao, J. Hu, Y. Duan, F. Pan, Nanoscale 10 (2017) 386.
[82] D.A. Stevens, J.R. Dahn, J. Electrochem. Soc. 148 (2001) A803–A811.
[83] J. Hu, Y. Jie, Y. Duan, C. Liu, P. Feng, Chem. Commun. 53 (2016) 857–860.
[84] J. Xue, Z. Ling, Z. Dou, Y. Yan, G. Yue, Z. Zhen, L. Cui, RSC Adv. 6 (2016) 110820.
[85] L. Bo, X. Zhang, H. Shioyama, T. Mukai, T. Sakai, X. Qiang, J. Power Sources 195 (2010) 857–861.
[86] S. Chen, R. Zhou, Y. Chen, Y. Fu, L. Ping, Y. Song, W. Li, J. Nanoparticle Res. 19 (2017) 127.
[87] R. Ding, J. Zhang, J. Qi, Z. Li, C. Wang, M. Chen, ACS Appl. Mater. Interf. 10 (2018) 13470–13478.
[88] Y. Liu, W. Wang, Q. Chen, C. Xu, D. Cai, H. Zhan, Inorg. Chem. 58 (2019) 1330–1338.
[89] R. Tan, J. Yang, J. Hu, K. Wang, Y. Zhao, F. Pan, Chem. Commun. 52 (2016) 986–989.
[90] A.L. Reddy, A. Srivastava, S.R. Gowda, H. Gullapalli, M. Dubey, P.M. Ajayan, ACS Nano 4 (2010) 6337.
[91] L. Lin, J. Wang, C. Wang, G. Wang, Appl. Surf. Sci. 390 (2016) 303–310.
[92] L. Wei, H.E. Karahan, S. Zhai, H. Liu, X. Chen, Z. Zhou, Y. Lei, Z. Liu, Y. Chen, Adv. Mater. 29 (2017) 1701410.
[93] J. Wu, H. Zhang, T. Yao, X. Zhang, Y. Lian, Chemistry 23 (2017).
[94] H. Yang, J. Xiao, L. Su, T. Feng, Q. Lv, X. Zhang, Chem. Commun. 53 (2017) 3882.
[95] M.B. Zakaria, RSC Adv. 6 (2016) 10341–10351.
[96] W. Xia, J. Masa, M. Bron, W. Schuhmann, M. Muhler, Electrochem. Commun. 13 (2011) 593–596.
[97] W. Gang, K.L. More, C.M. Johnston, Z. Piotr, Science 332 (2011) 443–447.
[98] M.Y. Chen, B. Lai, Y.F. Zhou, G.Q. Zhang, Adv. Mater. Res. 1051 (2014) 186–190.
[99] H.-C. Huang, C.-Y. Su, K.-C. Wang, H.-Y. Chen, Y.-C. Chang, Y.-L. Chen, K.C.W. Wu, C.-H. Wang, ACS Sustain. Chem. Eng. 7 (2019) 3185–3194.
[100] H. Che, Y.S. He, X.Z. Liao, H.J. Zhang, W. Zhang, Z.F. Ma, ChemistrySelect 2 (2017) 1854–1859.
[101] D. Su, M. Cortie, G. Wang, Adv. Energy Mater. 7 (2017) 1602014.
[102] Y. Song, Z. Li, K. Guo, T. Shao, Nanoscale 8 (2016) 15671–15680.
[103] L. Liu, S.D. Xu, Q. Yu, F.Y. Wang, H.L. Zhu, R.L. Zhang, X. Liu, Chem. Commun. 52 (2016) 11693.
[104] Y. Cao, L. Xiao, M.L. Sushko, W. Wang, B. Schwenzer, J. Xiao, Z. Nie, L.V. Saraf, Z. Yang, J. Liu, Nano Lett. 12 (2012) 3783–3787.
[105] C. Liu, J. Hu, L. Yang, W. Zhao, H. Li, F. Pan, Chem. Commun. 54 (2018) 2142.
[106] Y.V. Lim, W. Ye, G. Lu, D. Kong, R. Ang, J.I. Wong, Y.Y. Hui, J. Mater. Chem. A 5 (2017) 10406.
[107] W.S. Zhi, Y. Sun, Q. Zhang, Y. Cui, Chem. Soc. Rev. 45 (2016) 5605–5634.
[108] F.J. Maldonado-Hodar, C. Moreno-Castilla, J. Rivera-Utrilla, Y. Hanzawa, Y. Yamada, Langmuir 16 (2000) 4367–4373.
[109] F.C. Zheng, D.Q. Zhu, X.H. Shi, Q.W. Chen, J. Mater. Chem. A 3 (2015) 2815–2824.
[110] J.X. Shao, J.H. Feng, H. Zho, A.H. Yuan, Appl. Surf. Sci. 471 (2019) 745–752.

[111] Y. Hu, J.O. Jensen, W. Zhang, S. Martin, R. Chenitz, C. Pan, W. Xing, N.J. Bjerrum, Q.F. Li, J. Mater. Chem. A 3 (2015) 1752–1760.
[112] Q.C. Wang, Y.P. Lei, Z.Y. Chen, N. Wu, Y.B. Wang, B. Wang, Y.D. Wang, J. Mater. Chem. A 6 (2018) 516–526.
[113] Y. Wang, S.X. Bao, R. Li, G.Z. Zhao, Z.H. Wang, Z. Zhao, Q.W. Chen, ACS Appl. Mater. Interf. 7 (2015) 2088–2096.
[114] H.L. Jiang, B. Liu, T. Akita, M. Haruta, H. Sakurai, Q. Xu, J. Am. Chem. Soc. 131 (2009) 11302.
[115] J.F. Keggin, F.D. Miles, Nature 137 (1936) 278–577.
[116] F. Grandjean, L. Samain, G.J. Long, Dalton Trans. 45 (2016) 18018–18044.
[117] J.T. Chen, G.L. Xia, P. Jiang, Y. Yang, R. Li, R.H. Shi, J.W. Su, Q.W. Chen, ACS Appl. Mater. Interf. 8 (2016) 13378–13383.
[118] J.T. Chen, Y. Yang, J.W. Su, P. Jiang, G.L. Xia, Q.W. Chen, ACS Appl. Mater. Interf. 9 (2017) 3596–3601.
[119] P. Jiang, J.T. Chen, C.L. Wang, K. Yang, S.P. Gong, S. Liu, Z.Y. Lin, M.S. Li, G.L. Xia, Y. Yang, J.W. Su, Q.W. Chen, Adv. Mater. 30 (2018).
[120] J.W. Su, Y. Yang, G.L. Xia, J.T. Chen, P. Jiang, Q.W. Chen, Nat. Commun. 8 (2017) 14969.